A High-order Accurate Summation-by-Parts Finite Difference Method for Fully-dynamic Earthquake Sequence Simulations within Sedimentary Basins

Tobias W. Harvey [1], Brittany A. Erickson [1,2], Jeremy E. Kozdon [3]

[1]Department of Computer Science, University of Oregon, Eugene, Oregon
[2]Department of Earth Sciences, University of Oregon, Eugene, Oregon
[3]Department of Applied Mathematics, Naval Postgraduate School, Monterey, California

This manuscript has been submitted for publication in the Journal of Geophysical Research: Solid Earth. Please note that, despite having undergone peer-review, the manuscript has yet to be formally accepted for publication. Subsequent versions of this manuscript may have slightly different content. If accepted, the final version of this manuscript will be available via the 'Peer-reviewed Publication DOI' link on the right-hand side of this webpage. Please feel free to contact any of the authors; we welcome feedback.

Corresponding author: Tobias W. Harvey, `tharvey@cs.uoregon.edu`

Key Points:

- Non-stiff summation-by-parts finite difference methods can be derived for fully-dynamic earthquake sequence with rate-and-state friction.
- Long-term simulations of fully-dynamic earthquake sequences are sensitive to the switching criterion even with adequate resolution.
- Even with full dynamics present, sediments can act as barriers to rupture.

Abstract

We present a computationally efficient numerical method for earthquake sequences that incorporates wave propagation during rupture. A vertical strike-slip fault governed by rate-and-state friction is embedded in a heterogeneous elastic half-space discretized using a high-order accurate Summation-by-Parts finite difference method. We develop a two solver approach: Adaptive time-stepping is applied during the interseismic periods and during coseismic rupture we apply a non-stiff method, which enables a variety of explicit time stepping methods. We consider a shallow sedimentary basin and explore model sensitivity to spatial resolution and the switching criteria used to transition between solvers. For sufficient grid resolution and switching thresholds, simulations results remain robust over long time scales. We explore the effects of full dynamics on earthquake sequences, comparing outcomes to their quasi-dynamic counterparts. The fully-dynamic ruptures are accompanied with higher stress concentrations, faster slip rates and rupture speeds, and produce seismic scattering in the bulk as waves propagate through and reflect off the basin edges. Because single-event dynamic simulations penetrate further into sediments compared to quasi-dynamic simulations, we hypothesize that the incorporation of inertial effects would produce sequences of only surface-rupturing events, as opposed to the subbasin events that emerge in purely quasi-dynamic scenarios. However, we find that with full dynamics present, the alternating sequence of subbasin and surface breaking ruptures is a persistent outcome. Thus an earthquake's potential to penetrate into shallow sediments should be viewed through the lens of the earthquake sequence, as it depends strongly on self-consistent initial conditions obtained from seismogenic cycling.

Plain Language Summary

We have developed a robust and efficient modeling framework for simulating earthquake sequences that incorporates the important physics of seismic waves and heterogeneous materials. We consider earthquakes occurring on a strike slip fault cutting through a sedimentary basin and show that long-term modeling outcomes are sensitive to the numerical parameters of grid resolution and how we switch between solvers for the interseismic and coseismic phases. In addition, we compare fully-dynamic and quasi-dynamic model outcomes and show that when full dynamics are present, ruptures are much larger. However, like the quasi-dynamic scenario, events alternate between reaching the surface and remaining buried below the sedimentary basin. These results underscore the importance that earthquake rupture behavior is strongly dependent on initial conditions that have evolved over very long periods ($\sim$1000s of years).

1 Introduction

Numerical simulations of earthquake processes enable the exploration of how physical features such as fault friction, heterogeneous material properties, and initial stress conditions can give rise to the most destructive earthquakes. It is widely agreed that long-term models capable of simulating multiple earthquake cycles are necessary to better understand earthquake nucleation, aseismic slip, dynamic rupture and postsesimic afterslip, all the while incorporating complex geometries with realistic friction laws, and important physics such as full dynamics and material complexities (Lapusta et al., 2000; Erickson et al., 2020; Jiang et al., 2022). However, simulations with such features pose computational difficulties and modelers must often make simplifying assumptions to make simulations tractable. As Lapusta and Rice (2003) describe, the main computational burden in simulating multiple cycles arises from the drastically different spatial and temporal scales that must be resolved in a single simulation. In the spatial domain, fault depths and lengths range from tens to thousands of kilometers, while nucleation zones are realistically only a few meters. Temporally, slow tectonic loading of faults results in earthquakes with recurrence intervals of hundreds to thousands of years, with slip rates (during the fast coseismic periods) that evolve over fractions of a second. For instance, resolving coseismic wave propagation during rupture requires time steps on the order of seconds, but time-stepping schemes must be adaptive for long-term simulations (hundreds of years) to be feasible.

Within the modeling community a wide variety of computational frameworks for simulations of earthquakes exist that address the drastically different spatial and temporal scales of earthquake processes. Single-event dynamic rupture simulations have emerged as powerful tools for exploring the effects of complex fault geometry, friction, and off-fault plasticity on rupture and the associated damaging ground motion (e. g. Harris & Day, 1993; Duan & Oglesby, 2007; Dunham et al., 2011; Shi & Day, 2013; Ando & Kaneko, 2018; Harris et al., 2018). Such simulations focus on a single coseismic event, on regional spatial scales (hundreds of kilometers). A limitation of dynamic rupture simulations, however, is that artificial prestress conditions and *ad hoc* nucleation procedures must be used. In addition, since dynamic rupture simulations are inherently limited to the timescales of wave propagation (seconds to minutes), they cannot be used for long-term simulations nor to understand how a history of past earthquakes affects subsequent rupture. Alternatively, earthquake simulators model multiple cycles on very large spatial scales, such as the entirety of California, and are currently being used in hazard analysis contexts (Shaw et al., 2018; Tullis et al., 2012). To make such computations tractable however, simulators consider approximations to inertial effects, using enlarged cell sizes that do not always resolve physical length scales (Rice, 1993).

Sequences of Earthquakes and Aseismic Slip (SEAS) simulations on the other hand, make a compromise between dynamic rupture simulations and earthquake simulators, modeling long-term earthquake sequences on regional spatial scales with sufficient grid resolution, and incorporating increasingly more rigorous physics such as full dynamic effects (Erickson, Jiang, et al., 2022). Such cycle simulations not only present a method for better understanding the physics of nucleation, but explicitly simulate the stress conditions prior to large earthquakes, and uncover the long term behavior of earthquake processes over multiple cycles. Early SEAS simulations applied boundary element methods (BEM) which reduce the computational burden by restricting the degrees of freedom to only the fault and not the surrounding bulk (Lapusta et al., 2000). Recent developments based on BEM have considered the important features of fluid effects, viscoelasticity, shear heating, full dynamic wave propagation, and fault roughness (e. g. Noda & Lapusta, 2010; Thomas et al., 2014; Lambert & Barbot, 2016; Barbot, 2018; Cattania & Segall, 2021).

Although computationally efficient, a disadvantage of BEM-based methods are that material inelasticity and heterogeneity cannot easily be included, and these properties are known to play a crucial role in rupture dynamics (Ma & Andrews, 2010; Kozdon & Dunham, 2013; Bydlon & Dunham, 2015). Near fault material heterogeneities are of particular importance since they can act as barriers to rupture and generate higher frequency ground motion (Kagawa et al., 2004; Bydlon & Dunham, 2015). More recently, volume-based SEAS methods (which can readily incorporate material complexity) have been developed (Erickson & Dunham, 2014; Erickson et al., 2017; Allison & Dunham, 2018; Abdelmeguid et al., 2019). However, for computational efficiency these methods were restricted to quasi-dynamic simulations. Thomas et al. (2014) show that quasi-dynamic simulations systematically underestimate slip and slip-rate during rupture, and omit wave-mediated stress transfers, all of which motivate the development of fully-dynamic, volume-based SEAS methods (e.g. Kaneko et al., 2011; Duru et al., 2019; Thakur et al., 2020; Hajarolasvadi & Elbanna, 2017). These recent works are limited to second-order accurate time-stepping methods and/or low order of spatial accuracy. For example the work of Duru et al. (2019) develops a custom, second-order time stepping scheme to handle numerical stiffness introduced by rate-and-state friction. However, higher-order temporal discretizations for applications requiring high levels of resolution have been found to be more computationally efficient as error tolerances become more stringent, and can capture temporal characteristics of rapidly evolving dynamics more easily (Kreiss & Oliger, 1972). High-order spatial accuracy, on the other hand, is desirable for increased spatial resolution and, particularly for wave propagation, its superior handling of errors induced by numerical dispersion (Oh, 2012).

In this work we develop a non-stiff, computationally efficient method for SEAS simulations that incorporates full dynamics during rupture. We develop a two solver approach which includes high-order spatial accuracy and allows for the use of generic, explicit time stepping schemes of arbitrary order temporal accuracy during coseismic rupture. During both the coseismic and interseismic phases we apply a high-order accurate Summation-by-Parts (SBP) finite difference spatial discretization with boundary conditions imposed through the simultaneous-approximation-term (SAT) technique; solvers for both phases are based on the non-stiff method of Erickson, Kozdon, and Harvey (2022). Inertial effects are approximated with radiation damping during the interseismic periods, and use the adaptive time stepping method of Erickson and Dunham (2014). We then opt, in the coseismic phase, to apply a 4th-order, low-storage Runge-Kutta scheme with a fixed time step from Carpenter and Kennedy (1994).

As pointed out by Duru et al. (2019), the second-order form of the wave equation (as opposed to the velocity-stress formulation of the first order form) is desirable for the interseismic phase. Therefore in both the interseismic and coseismic regimes we solve the governing equations in second-order form, allowing for a straight-forward transition between solvers. We conduct rigorous spatial convergence tests of our numerical method using the method of manufactured solutions (Roache, 1998) and determine constraints on computational parameters defining grid resolution and the switching criteria (used to switch between solvers), so that solutions from different simulations remain the same over many cycles.

We revisit the quasi-dynamic simulations of Erickson and Dunham (2014) to explore the influence of full dynamics on both individual ruptures and the long-term features of the earthquake cycle when a shallow sedimentary basin is present. As in this previous study, we isolate the effects of elastic heterogeneity, neglecting possible correlations between lithology and frictional properties which might suggest using velocity-strengthening properties within the basin; see Erickson and Dunham (2014) for more details. We hypothesize that the addition of full dynamics produces a higher frequency of surface rupturing events compared to the alternating sequences involving subbasin ruptures observed in Erickson and Dunham (2014), as evidence points towards dynamic rupture's ability to penetrate farther into regions that inhibit slip such as velocity-weakening friction and/or more compliant material (Kozdon et al., 2012; Hirono et al., 2019; Lambert & Lapusta, 2021). However, we find instead that the long term limit cycle alternates in a similar manner, albeit with much larger surface breaking ruptures. We also conduct single-event simulations illustrating how full-dynamics promote surface-rupturing events compared to otherwise (i.e. quasi-dynamic) subbasin ruptures. These findings underscore the importance of viewing rupture potential into sedimentary regions not as a stand-alone event, but rather strongly influenced by initial conditions obtained from a long history of seismogenic cycling. In addition, these alternating sequences that emerge, even with full dynamics present, provide further insight into what might occur in subduction zones, where large events may terminate below the accretionary prism and only occasionally break through to the trench (e.g. the 2011 Tohoku-oki earthquake).

The rest of the paper is organized as follows: The two dimensional governing equations for our problem are described in Section 2. Section 3 explains how we use a coordinate transform to simultaneously spatially resolve portions of the domain requiring higher resolution, and maintain a computationally efficient method. Section 4 describes the construction of the SBP operators used in the spatial discretization. Section 5 discusses the application of the SBP operators to the continuous problem to form a semi-discretization, and details the time-stepping methods used. Section 6 outlines the convergence tests we developed for the interseismic and coseismic discretetizations. Section 7 explores the dependency of solutions on computational parameters and Section 8 addresses the addition of full dynamics to the sedimentary basin simulations of Erickson and Dunham (2014). A discussion is included in Section 9.

2 Governing Equations

We consider a heterogeneous, isotropic, linear elastic half-space defined by $(x, y, z) \in (-L_x, L_x)\times(-\infty, \infty)\times(0, L_z)$ (z positive downward) with a free surface at $z = 0$. We assume antiplane shear deformation where the only non-zero component of particle displacement $u(x, z, t)$ is in the y-direction, and depends only on $(x, z) \in \Omega = (-L_x, L_x)\times(0, L_z)$ and the only non-zero perturbations to the stress tensor are σ_{xy} and σ_{yz}. A vertical strike-slip fault is embedded in the $x = 0$ plane. Substituting Hooke's law into conservation of momentum results in the 2D elastodynamic wave equation

$$\rho(x,z)\ddot{u} = \frac{\partial}{\partial x}\left[\mu(x,z)\frac{\partial u}{\partial x}\right] + \frac{\partial}{\partial z}\left[\mu(x,z)\frac{\partial u}{\partial z}\right] + S(x,z,t), \quad (x,z) \in \Omega \quad t \geq 0, \qquad (1)$$

where ρ is the material density, μ is the shear modulus, and S is a body force.

Governing equation (1) must be supplemented with well-posed initial, boundary, and interface conditions. For computational ease, in this work we assume these conditions contain symmetries about $x = 0$, such that the displacement field is anti-symmetric about the fault (i.e. $u(x^+, z, t) = -u(x^-, z, t)$), allowing us to consider a "one-sided" problem. Therefore, we need only solve the corresponding problem in the quarter-space $\Omega_0 = (0, L_x) \times (0, L_z)$. Boundary conditions must be supplied at all four boundaries, and for notational ease in what follows, we denote these with the following conventions: $x = 0$ (the fault) is boundary 1, $x = L_x$ (the remote boundary) is boundary 2, Earth's free surface ($z = 0$) is boundary 3, and the boundary at depth ($z = L_z$) is boundary 4.

We consider the elastodynamic equation (1) during the coseismic phases. During the interseismic phases we consider the equilibrium equation (where the left hand side of (1) is set to zero), but include approximate inertial effects through radiation-damping (Rice, 1993). Although this is technically a "quasi-dynamic" approach, in this work we reserve this phrase for earthquake sequence simulations that use the radiation damping approximation throughout the simulation, including the coseismic phase. We can therefore discuss and compare model outcomes that are either "fully-dynamic" or "quasi-dynamic", even though fully-dynamic simulations apply radiation damping during the interseismic periods. Throughout this work we also refer to coseismic and interseismic solvers. These refer to the numerical techniques used for the fully-dynamic phases and the phases where the equilibrium equation is solved and radiation damping is applied, respectively. In the next sections we provide details of the initial and boundary conditions for each regime, using general boundary and initial data for clarity of the numerical methods that follow. However, we describe in later sections specifics of the boundary data and how the two computational techniques are integrated for fully-dynamic earthquake cycle simulations.

2.1 Initial and Boundary Conditions

2.1.1 Rate-and-State Friction

The jump in displacement across the fault is known as fault slip. Because we consider a one-sided problem in this work, slip is denoted by $\delta(z, t) = 2u(0, z, t)$, with slip rate denoted V, namely

$$\dot{\delta} = V. \qquad (2)$$

At the fault boundary ($x = 0$) we impose the condition that shear stress τ_s (defined explicitly in later sections) is equal to fault strength $F(V, \psi)$, namely

$$\tau_s = F(V, \psi), \tag{3}$$

where $F(V, \psi) = \bar{\sigma}_n f(V, \psi)$ for effective normal stress $\bar{\sigma}_n$ and rate-and-state dependent friction coefficient f (Dieterich, 1979). Here ψ is an experimentally motivated state variable (Marone, 1998). We adopt the regularized form for f, namely,

$$f(V, \psi) = a \sinh^{-1}\left(\frac{V}{2V_0} e^{\frac{\psi}{a}}\right) \tag{4}$$

(Lapusta et al., 2000) and assume that the state variable evolves in time according to the aging law

$$\dot{\psi} = G(V, \psi) = \frac{bV_0}{L} e^{\frac{f_0 - \psi}{b} - \frac{|V|}{V_0}}. \tag{5}$$

Here, a and b are dimensionless empirical parameters corresponding to the direct and evolution effects, respectively, and determine if the fault is velocity strengthening ($a - b > 0$), or velocity weakening ($a - b < 0$) (Marone, 1998). f_0 is a reference friction coefficient for reference slip rate V_0, and L is the characteristic slip distance.

The fault interface at $x = 0$ is subject only to the rate-and-state friction boundary condition (3). The fault boundary condition manifests as a displacement (Dirichlet) boundary condition during the interseismic phase, and as a characteristic condition during the coseismic phase. For clarity of the numerical techniques, we state all boundary conditions for general boundary data. In Section 6, however, we provide specific details relevant to our earthquake cycle simulations (including rate-and-state friction) and how they give rise to these boundary conditions and supply the boundary data.

2.1.2 Conditions for the Interseismic Phase

During the interseismic phase, the left-hand side of (1) is set to zero, resulting in an elliptic problem for particle displacements u. Time-dependent boundary conditions on traction are imposed at $z = 0$ and $z = L_z$ and on displacement at $x = 0$ and at $x = L_x$, namely

$$\begin{aligned}
u &= g_q^1(z, t), & x &= 0, & \text{(6a)}\\
u &= g_q^2(z, t), & x &= L_x, & \text{(6b)}\\
\tau &= g_q^3(x, t), & z &= 0, & \text{(6c)}\\
\tau &= g_q^4(x, t), & z &= L_z, & \text{(6d)}
\end{aligned}$$

where the traction τ on any boundary can be computed using the formula

$$\tau = \begin{bmatrix} n_x & n_z \end{bmatrix} \begin{bmatrix} \mu \frac{\partial u}{\partial x} \\ \mu \frac{\partial u}{\partial z} \end{bmatrix}, \tag{7}$$

where $n = [n_x \ n_z]^T$ is the outward pointing normal to a boundary. Generic boundary data $g_q^1, g_q^2, g_q^3, g_q^4$ correspond to boundaries 1-4 during the interseismic phase.

2.1.3 Conditions for the Coseismic Phase

When full dynamics are present, two initial conditions must be supplied, namely

$$\begin{aligned}
u(x, z, 0) &= u_0(x, z), & & \text{(8a)}\\
\dot{u}(x, z, 0) &= v_0(x, z), \quad (x, z) \in \Omega_0. & & \text{(8b)}
\end{aligned}$$

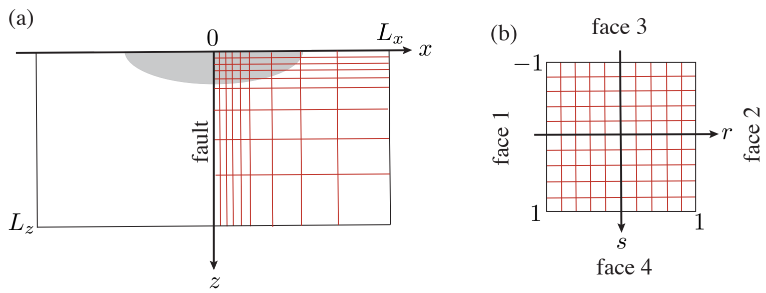

Figure 1. (a) The one-sided physical domain $(x, z) \in [0, L_x] \times [0, L_z]$ with a grid stretching and variable material parameters (illustrated by the gray semi-ellipse idealizing a sedimentary basin) is mapped to (b) the computational domain $(r, s) \in [-1, 1] \times [-1, 1]$ where constant grid spacing is used. The coordinate transform enables a smaller grid spacing near the fault and the free surface, as detailed in Appendix A; face numbering in the computational domain also shown.

We impose a traction boundary condition at $z = 0$ and all other boundaries assume a boundary condition on the incoming characteristic variable $Z\dot{u}+\tau$, where $Z = \sqrt{\mu\rho}$ is the shear impedance. The latter choice is necessary to avoid numerical stiffness (Erickson, Kozdon, & Harvey, 2022). The boundary conditions are thus given by

$$Z\dot{u} + \tau = R^1(Z\dot{u} - \tau) + g_d^1(z, t), \qquad x = 0, \tag{9a}$$
$$Z\dot{u} + \tau = R^2(Z\dot{u} - \tau) + g_d^2(z, t), \qquad x = L_x, \tag{9b}$$
$$\tau = g_d^3(x), \qquad z = 0, \tag{9c}$$
$$Z\dot{u} + \tau = R^4(Z\dot{u} - \tau) + g_d^4(x, t), \qquad z = L_z. \tag{9d}$$

Generic boundary data g_d^1, g_d^2, g_d^3 and g_d^4 denote data at boundaries 1-4 during the coseismic phase. $R^{1,2,4} \in [-1, 1]$ are reflection coefficients multiplying the outgoing characteristic variable $Z\dot{u}-\tau$ and can be set to different values at each boundary to enable different boundary condition types; for example setting $R = -1$ corresponds to a condition on velocity, while $R = 1$ specifies a traction conditions and $R = 0$ defines a nonreflecting boundary condition. As will be shown in Section 5.2.1, rate-and-state friction can also be enforced in this characteristic manner and implicitly defines a particular choice of R^1, which is both temporally and spatially varying.

3 Domain Transformation

In many scientific applications it is often desirable to have increased spatial resolution in some parts of the domain, while maintaining a coarser grid elsewhere, for computational efficiency. Here we accomplish this through a coordinate transformation between the physical domain Ω_0 and a computational domain $\bar{\Omega} = \{(r(x, y), s(x, y)) : -1 \le r, s \le 1\}$ which allows us to place more nodes in regions which require higher resolution. The computational boundaries, known as faces, are denoted using the conventions: $f = 1$ (face 1) is the $r = -1$ boundary, $f = 2$ is the $r = 1$ boundary, $f = 3$ is the $s = 1$ boundary, and $f = 4$ is the $s = -1$ boundary; see Figure 1. Additionally, we maintain the convention that $f = 1$ maps to boundary 1 ($x = 0$), $f = 2$ maps to the remote boundary 2 ($x = L_x$), $f = 3$ maps to the surface (boundary 3, at $z = 0$), and $f = 4$ maps to the depth boundary 4 ($z = L_z$) (i.e. transformations are conforming). The governing equations are mapped to the computational domain, where finite difference approximations are made, then transformed back to the physical domain.

We let J denote the Jacobian determinant of the transformation, namely,

$$J = \frac{\partial x}{\partial r}\frac{\partial z}{\partial s} - \frac{\partial z}{\partial r}\frac{\partial x}{\partial s}. \tag{10}$$

The isotropic problem (1) in physical space can be recast as an anisotropic problem in the computational domain under a coordinate transformation as

$$J\rho\ddot{u} = \begin{bmatrix}\frac{\partial}{\partial r} & \frac{\partial}{\partial s}\end{bmatrix} C \begin{bmatrix}\frac{\partial u}{\partial r} \\ \frac{\partial u}{\partial s}\end{bmatrix} + JS(r,s), \tag{11}$$

where C is a 2×2 matrix-valued function with components

$$C_{ij}(r,s) = J\left(\frac{\partial i}{\partial x}\mu\frac{\partial j}{\partial x} + \frac{\partial i}{\partial z}\mu\frac{\partial j}{\partial z}\right), \qquad i,j \in \{r,s\}. \tag{12}$$

The computational traction on face f is

$$\hat{\tau} = \begin{bmatrix}\hat{n}_r^f & \hat{n}_s^f\end{bmatrix} C \begin{bmatrix}\frac{\partial u}{\partial r} \\ \frac{\partial u}{\partial s}\end{bmatrix} = S_J\tau, \tag{13}$$

where $\hat{n}_r^f$ and $\hat{n}_s^f$ are components of the outward-pointing normal vector to face f in the r and s directions and S_J is the surface Jacobian satisfying the relationships

$$S_J n_1 = J\frac{\partial r}{\partial x}\hat{n}_1 + J\frac{\partial s}{\partial x}\hat{n}_2, \tag{14a}$$

$$S_J n_2 = J\frac{\partial r}{\partial z}\hat{n}_1 + J\frac{\partial s}{\partial z}\hat{n}_2. \tag{14b}$$

Under this transformation, boundary conditions (6c)-(6d) during the interseismic phase become

$$\hat{\tau} = S_J g_q^3(x,t), \qquad s = -1, \tag{15a}$$

$$\hat{\tau} = S_J g_q^4(x,t), \qquad s = 1, \tag{15b}$$

and for the dynamic problem

$$\hat{Z}\dot{u} + \hat{\tau} = R^1(\hat{Z}\dot{u} - \hat{\tau}) + S_J g_d^1(z,t), \qquad r = -1, \tag{16a}$$

$$\hat{Z}\dot{u} + \hat{\tau} = R^2(\hat{Z}\dot{u} - \hat{\tau}) + S_J g_d^2(z,t), \qquad r = 1, \tag{16b}$$

$$\hat{\tau} = S_J g_d^3(x,t), \qquad s = -1, \tag{16c}$$

$$\hat{Z}\dot{u} + \hat{\tau} = R^4(\hat{Z}\dot{u} - \hat{\tau}) + S_J g_d^4(x,t), \qquad s = 1, \tag{16d}$$

where $\hat{Z} = S_J Z$.

4 SBP Finite Difference Operators and Spatial Discretization

During the interseismic phase, we set the left-hand side of (1) to zero and enforce boundary conditions (6). During the coseismic phase we solve the initial-boundary-value problem defined by (1), (8), (9). Numerically, equations in both regimes are solved in the computational domain $\bar{\Omega}$ which is discretized with SBP operators. SBP operators are finite difference operators that discretely approximate derivatives and mimic integration-by-parts identities. In conjunction with boundary enforcement through the simultaneous-approximation-term (SAT) technique, these operators produce a discrete energy estimate that can be used to prove discrete conservation of energy, and stability as an analogue to conservation of energy, and stability of the continuous problem (Svärd & Nordström, 2013). We first define 1D SBP operators, as they are used to construct the 2D SBP operators.

4.1 One Dimensional Operators

Let the domain $-1 \leq r \leq 1$ be partitioned with $N+1$ equally spaced nodes so that the distance between each node is $h = 2/N$. We denote the projection of a function u onto the resulting grid points as $\boldsymbol{u}^T = \left[u_0, u_1, \cdots u_{n+1}\right]$. We also define the restriction operator $\boldsymbol{e}_k^T$, which takes a grid function to its value at $r(hk)$, as a vector of zeros except for a one at the kth index. While sometimes these operators are useful, they can be cumbersome, so we use them interchangeably with $\boldsymbol{e}_k^T \boldsymbol{u} = u_k$. A first derivative operator $\boldsymbol{D}_r$ is a diagonal SBP operator if

$$\boldsymbol{D}_r = \boldsymbol{H}^{-1}\boldsymbol{Q} \approx \frac{\partial}{\partial r}, \tag{17}$$

with

$$\boldsymbol{Q} + \boldsymbol{Q}^T = \begin{bmatrix} -1 & & & & \\ & 0 & & & \\ & & \ddots & & \\ & & & 0 & \\ & & & & 1 \end{bmatrix}, \tag{18}$$

where $\boldsymbol{H}$ is a diagonal quadrature matrix defining a norm $||u||_H^2 = \boldsymbol{u}^T\boldsymbol{H}\boldsymbol{u}$ (Hicken & Zingg, 2013). The decomposition in (17) yields the identity

$$\boldsymbol{u}^T\boldsymbol{D}_r\boldsymbol{v} = u_N v_N - u_0 v_0 - \boldsymbol{u}^T\boldsymbol{D}_r^T\boldsymbol{v}, \tag{19}$$

which is the discrete analog to the integration-by-parts identity

$$\int_{-1}^{1} u\frac{\partial v}{\partial r}dr = uv|_{-1}^{1} - \int_{-1}^{1}\frac{\partial u}{\partial r}v. \tag{20}$$

A variable coefficient, second derivative operator $\boldsymbol{D}_{rr}^{(C)} \approx \frac{\partial}{\partial r}\left[C(r)\frac{\partial}{\partial r}\right]$ is an SBP operator if

$$\boldsymbol{D}_{rr}^{(C)} = \boldsymbol{H}^{-1}(-\boldsymbol{A}^{(C)} + C_N\boldsymbol{e}_N\boldsymbol{b}_N^T - C_0\boldsymbol{e}_0\boldsymbol{b}_0^T), \tag{21}$$

where $\boldsymbol{A}^{(C)}$ is a positive-definite matrix. Vector $\boldsymbol{b}_k^T$ computes an approximation to the first derivative at grid point k, and is not necessarily the first and last row of $\boldsymbol{D}_1$ (Mattsson & Parisi, 2010). We opt to use this construction of $\boldsymbol{D}_{rr}^{(C)}$ instead of an application of the first derivative twice since this technique increases the stencil width so that the highest mode (π-mode) on the grid is not captured (Mattsson & Nordström, 2004). SBP property (21) then leads to the identity

$$\boldsymbol{u}^T\boldsymbol{H}\boldsymbol{D}_{rr}^{(C)}\boldsymbol{v} = C_N u_N\boldsymbol{b}_N^T\boldsymbol{v} - C_0 u_0\boldsymbol{b}_0^T\boldsymbol{v} - \boldsymbol{u}^T\boldsymbol{A}^{(C)}\boldsymbol{v}, \tag{22}$$

which is the discrete analog to the continuous integration-by-parts identity

$$\int_{-1}^{1} u\frac{\partial}{\partial r}\left(C\frac{\partial v}{\partial r}\right)dr = uC\frac{\partial v}{\partial r}\bigg|_{-1}^{1} - \int_{-1}^{1}\frac{\partial u}{\partial r}C\frac{\partial v}{\partial r}. \tag{23}$$

4.2 Two Dimensional Operators

Describing 2D operators poses some notational challenges. We therefore hold the following conventions: Vector subscripts indicate an indexing into that vector. For matrix operators a subscript denotes the direction(s) in which that operator acts. A matrix superscript, if there is a colon, denotes the grid line in which one row or column of the grid is held fixed. If there is no colon, it denotes the face f that that matrix is acting on. If there are parentheses around the superscript it denotes the function in that superscript is incorporated into that operator. Lastly, for more clarity on operator dimensions refer to Table 1.

We describe the operators on $\bar{\Omega}$, and let the domain be discretized with $N+1$ equally spaced grid points in each direction, a distance of $h = 2/N$ apart. Note that discretizing with the same number of grid points in each direction is not necessary in general, however it simplifies the presentation. The projection of u onto the grid is $\boldsymbol{u}^T = \begin{bmatrix} u_{00} & \dots & u_{N0} \dots u_{0N} & \dots & u_{NN} \end{bmatrix}$, where $u_{kl} \approx u(kh, lh)$ and is stored as a vector with r being the fastest index. The 2D operators are constructed via the Kronecker product:

$$\boldsymbol{A} \otimes \boldsymbol{B} = \begin{bmatrix} a_{11}\boldsymbol{B} & \dots & a_{1n}\boldsymbol{B} \\ \vdots & \ddots & \vdots \\ a_{m1}\boldsymbol{B} & \dots & a_{mn}\boldsymbol{B} \end{bmatrix}, \tag{24}$$

which orients 2D matrices to operate on 2D vectors with respect to its stacking order. We define the face restriction operators that take a volume vector to a face vector as:

$$\bar{\boldsymbol{L}}^1 = \boldsymbol{I} \otimes \boldsymbol{e}_0^T, \qquad \bar{\boldsymbol{L}}^2 = \boldsymbol{I} \otimes \boldsymbol{e}_N^T, \qquad \bar{\boldsymbol{L}}^3 = \boldsymbol{e}_0^T \otimes \boldsymbol{I}, \qquad \bar{\boldsymbol{L}}^4 = \boldsymbol{e}_0^T \otimes \boldsymbol{I}, \tag{25}$$

where $\boldsymbol{I}$ is the $(N+1) \times (N+1)$ identity matrix. More generally, the restriction to a single grid line l in the r and s directions are:

$$\bar{\boldsymbol{L}}^{l:} = \boldsymbol{e}_l^T \otimes \boldsymbol{I}, \qquad \bar{\boldsymbol{L}}^{:r} = \boldsymbol{I} \otimes \boldsymbol{e}_r^T. \tag{26}$$

Higher-dimensional second derivative operators also require the construction of positive-definite interior second derivative matrices $\tilde{\boldsymbol{A}}_{rr}^{(C_{rr})}$, $\tilde{\boldsymbol{A}}_{ss}^{(C_{ss})}$, $\tilde{\boldsymbol{A}}_{rs}^{(C_{rs})}$ and $\tilde{\boldsymbol{A}}_{sr}^{(C_{sr})}$. For each grid line, the 1D operator $\boldsymbol{A}^{(C)}$ is constructed and placed in the correct section of the larger 2D matrix (expanding a single second derivative matrix with the Kronecker product and the identity matrix only works in the constant coefficient case). To better illustrate this construction, it is useful to define $\tilde{\boldsymbol{C}}_{ij} = \operatorname{diag}(\boldsymbol{c}_{ij})$ where $\boldsymbol{c}_{ij}$ is the projection of $C_{ij}(r,s)$ onto the grid, and denote the coefficients along the individual grid lines as

$$\boldsymbol{C}_{ij}^{:l} = \operatorname{diag}(C_{ij}(0,hl), \dots, C_{ij}(hN,hl)), \qquad \boldsymbol{C}_{ij}^{l:} = \operatorname{diag}(C_{ij}(hl,0), \dots, C_{ij}(hl,hN)). \tag{27}$$

The 2D operators can then be defined as the sum of 1D operators along each grid line, namely,

$$\tilde{\boldsymbol{A}}_{rr}^{(C_{rr})} = (\boldsymbol{H} \otimes \boldsymbol{I}) \left[\sum_{l=0}^{N} \left(\bar{\boldsymbol{L}}^{:l} \right)^T \boldsymbol{A}^{(\boldsymbol{C}_{rr}^{:l})} \bar{\boldsymbol{L}}^{:l} \right], \tag{28a}$$

$$\tilde{\boldsymbol{A}}_{ss}^{(C_{ss})} = (\boldsymbol{I} \otimes \boldsymbol{H}) \left[\sum_{k=0}^{N} \left(\bar{\boldsymbol{L}}^{k:} \right)^T \boldsymbol{A}^{(\boldsymbol{C}_{ss}^{k:})} \bar{\boldsymbol{L}}^{k:} \right], \tag{28b}$$

and the mixed derivative operators are given by

$$\tilde{\boldsymbol{A}}_{rs}^{(C_{rs})} = (\boldsymbol{I} \otimes \boldsymbol{Q}^T) \tilde{\boldsymbol{C}}_{rs} (\boldsymbol{Q} \otimes \boldsymbol{I}), \tag{28c}$$

$$\tilde{\boldsymbol{A}}_{sr}^{(C_{sr})} = (\boldsymbol{Q}^T \otimes \boldsymbol{I}) \tilde{\boldsymbol{C}}_{sr} (\boldsymbol{I} \otimes \boldsymbol{Q}). \tag{28d}$$

The boundary derivatives parallel to a face f are given with the one-dimensional first derivative operators

$$\bar{\boldsymbol{B}}_s^1 = \boldsymbol{D}_s \otimes \boldsymbol{e}_0^T, \tag{29a}$$

$$\bar{\boldsymbol{B}}_s^2 = \boldsymbol{D}_s \otimes \boldsymbol{e}_N^T, \tag{29b}$$

$$\bar{\boldsymbol{B}}_r^3 = \boldsymbol{e}_0^T \otimes \boldsymbol{D}_r, \tag{29c}$$

$$\bar{\boldsymbol{B}}_r^4 = \boldsymbol{e}_N^T \otimes \boldsymbol{D}_r, \tag{29d}$$

Operator	Dimensions
$\boldsymbol{e}_k$, $\boldsymbol{b}_k$	$(N+1)\times 1$
$\boldsymbol{Q}$, $\boldsymbol{D}_1$,$\boldsymbol{D}_2$,$\boldsymbol{H}$,$\boldsymbol{C}^{:}$	$(N+1)\times(N+1)$
$\boldsymbol{L}^{:}$,$\boldsymbol{B}^f$	$(N+1)\times(N+1)^2$
$\boldsymbol{A}_{ij}^{C_{ij}}$, $\boldsymbol{D}_{ij}^{C_{ij}}$, $\boldsymbol{C}_{ij}$	$(N+1)^2\times(N+1)^2$

Table 1. Dimensions of 2D operators using $N+1$ nodes in either direction.

and those perpendicular to the boundary use the first derivative operators $\boldsymbol{b}_0$ and $\boldsymbol{b}_N$ from the 1D second derivative operator

$$\bar{\boldsymbol{B}}_r^1 = \boldsymbol{I} \otimes \boldsymbol{b}_0^T, \tag{30a}$$
$$\bar{\boldsymbol{B}}_r^2 = \boldsymbol{I} \otimes \boldsymbol{b}_N^T, \tag{30b}$$
$$\bar{\boldsymbol{B}}_s^3 = \boldsymbol{b}_0^T \otimes \boldsymbol{I}, \tag{30c}$$
$$\bar{\boldsymbol{B}}_s^4 = \boldsymbol{b}_N^T \otimes \boldsymbol{I}. \tag{30d}$$

The full 2D second derivative operators (that include boundary closures) are then defined as

$$\tilde{\boldsymbol{D}}_{ij}^{(C_{ij})} = (\boldsymbol{H}\otimes\boldsymbol{H})^{-1}\left[-\tilde{\boldsymbol{A}}_{ij}^{(C_{ij})} + \sum_{f=2i-1}^{2i} \hat{n}_i^f (\bar{\boldsymbol{L}}^f)^T \boldsymbol{H}\boldsymbol{C}_{ij}^f \bar{\boldsymbol{B}}_j^f\right] \approx \frac{\partial}{\partial i} C_{ij} \frac{\partial}{\partial j}. \tag{31}$$

Lastly, gathering the face quadrature, variable coefficients, and boundary derivatives yields a single operator on each face, that will be used later to enforce boundary conditions, given by

$$\bar{\boldsymbol{G}}^f = \hat{n}_i^f \boldsymbol{H}\boldsymbol{C}_{ij}^f \bar{\boldsymbol{B}}_j^f, \tag{32}$$

where summation over i and j is implied. Operator $\bar{\boldsymbol{G}}^f$ is the discrete analog of the integral along a face of the C-weighted boundary derivative, which relates to traction (13), via

$$\boldsymbol{v}^T (\bar{\boldsymbol{L}}^f)^T \bar{\boldsymbol{G}}^f \boldsymbol{u} \approx \int_f v \hat{\tau}^f \, d\bar{\Omega}. \tag{33}$$

Applying the 2D SBP operators from this section, the transformed governing equation (11) is spatially discretized using the energy stable method from Erickson, Kozdon, and Harvey (2022):

$$\begin{aligned} \boldsymbol{J}(\boldsymbol{H}\otimes\boldsymbol{H})\boldsymbol{\rho}\ddot{\boldsymbol{u}} = &-(\tilde{\boldsymbol{A}}_{ij}^{(C_{ij})})\boldsymbol{u} + \sum_{f=1}^{4} (\bar{\boldsymbol{L}}^f)^T \boldsymbol{H}^f \hat{\boldsymbol{\tau}}^{*f} \\ &- \sum_{f=1}^{4} (\bar{\boldsymbol{G}}^f)^T (\boldsymbol{u}^{*f} - \bar{\boldsymbol{L}}^f \boldsymbol{u}) + \boldsymbol{J}\boldsymbol{S}. \end{aligned} \tag{34}$$

Here $\hat{\boldsymbol{\tau}}^{*f}$ and $\boldsymbol{u}^{*f}$ are numerical fluxes which are used as target values to impose boundary conditions on each of the four faces, $\boldsymbol{J}$ is the diagonal matrix of the grid projection of the Jacobian J, and $\boldsymbol{S}$ is the grid projection of the source function S.

5 Boundary Data and Time-Stepping

We now provide specifics for the boundary conditions considered in our earthquake sequence applications for both the interseismic and coseismic phases, along with details of time-stepping and switching between solvers.

5.1 The Interseismic Phase

During the interseismic phase we impose slow loading at rate V_p at the remote boundary, Earth's free surface lies at $z = 0$, and we assume a traction-free condition at depth $z = L_z$. At the fault we impose a Dirichlet condition of half the slip $\delta(z,t)$. These assumptions amount to boundary data,

$$g_q^1(z,t) = \delta(z,t)/2, \tag{35a}$$
$$g_q^2(z,t) = V_p t/2, \tag{35b}$$
$$g_q^3(x,t) = 0, \tag{35c}$$
$$g_q^4(x,t) = 0. \tag{35d}$$

The slip imposed at the fault in (35a) is obtained from the rate-and-state friction equation (3). During the interseismic phase we approximate inertial effects using radiation damping (Rice, 1993), where the shear stress on the fault is equal to the sum of the quasi-static shear stress and the radiation damping stress, namely

$$\tau_s = \tau^{qs} - \eta V, \tag{36}$$

where $\tau^{qs} = \sigma_{xy}(0,z,t)$ and $\eta = \mu/2c_s$. Specifics of how this relation determines the slip in (35a) is detailed in the time-stepping technique outlined below.

Under the domain transformation, the frictional relationship equating shear stress with fault strength is given by

$$\hat{\tau} - S_J \eta V = S_J F(V,\psi). \tag{37}$$

Numerically, boundary conditions during the interseismic phase are enforced by making the following choices for the numerical fluxes: For Dirichlet boundaries (faces 1 and 2), the data are interpolated onto the grid vector $\boldsymbol{g}_q^f$ and the fluxes are set to

$$\boldsymbol{u}^{*f} = \boldsymbol{g}_q^f \tag{38a}$$
$$\hat{\boldsymbol{\tau}}^{*f} = \hat{\boldsymbol{\tau}}^f, \tag{38b}$$

for $f = 1, 2$, where the numerical traction $\hat{\boldsymbol{\tau}}^f$ is the discrete version of continuous traction $\hat{\tau}^f$, and is computed as

$$\hat{\boldsymbol{\tau}}^f = (\boldsymbol{H}^f)^{-1}\bar{\boldsymbol{G}}^f \boldsymbol{u} + (\hat{n}_i^f \boldsymbol{C}_{ij}^f \hat{n}_i^f \boldsymbol{\Gamma}^f)(\boldsymbol{u}^{*f} - \boldsymbol{L}^f \boldsymbol{u}), \tag{39}$$

where $\boldsymbol{\Gamma}$ is a diagonal matrix of penalty terms given in Erickson, Kozdon, and Harvey (2022, Appendix B).

For the traction-free (Neumann) boundaries (faces 3 and 4), we choose numerical fluxes

$$\boldsymbol{u}^{*f} = \bar{\boldsymbol{L}}^f \boldsymbol{u}^f, \tag{40a}$$
$$\hat{\boldsymbol{\tau}}^{*f} = \boldsymbol{S}_J^f \boldsymbol{g}_q^f, \tag{40b}$$

for $f = 3, 4$. Here $\boldsymbol{S}_J^f$ is the grid projection of the surface Jacobian on face f. These choices for the fluxes correspond to standard SAT implementations of boundary conditions like that of Mattsson et al. (2009) and Erickson and Dunham (2014), but with the updated penalty parameters of Almquist and Dunham (2020). Substituting the numerical fluxes into discretization (34) yields the linear system

$$\left(\tilde{\boldsymbol{A}}_{ij}^{(C_{ij})} + \sum_{f=1}^{4} \bar{\boldsymbol{Q}}^f\right)\boldsymbol{u} = \sum_{f=1}^{4} \bar{\boldsymbol{K}}^f \boldsymbol{g}_q^f + \boldsymbol{J}\boldsymbol{S}, \tag{41}$$

with matrices

$$\bar{\boldsymbol{Q}}^f = -(\bar{\boldsymbol{L}}^f)^T \bar{\boldsymbol{G}}^f - (\bar{\boldsymbol{G}}^f)^T \bar{\boldsymbol{L}}^f + (\bar{\boldsymbol{L}}^f)^T \boldsymbol{H}^f \boldsymbol{C}_{11}^f \boldsymbol{\Gamma}^f, \qquad f = 1, 2, \tag{42a}$$

$$\bar{\boldsymbol{K}}^f = -(\bar{\boldsymbol{G}}^f)^T + (\bar{\boldsymbol{L}}^f)^T \boldsymbol{H}^f \boldsymbol{C}_{11}^f \boldsymbol{\Gamma}^f, \qquad f = 1, 2, \tag{42b}$$

and

$$\bar{\boldsymbol{Q}}^f = \boldsymbol{0}, \qquad f = 3, 4, \tag{43a}$$

$$\bar{\boldsymbol{K}}^f = (\bar{\boldsymbol{L}}^f)^T \boldsymbol{H}^f \boldsymbol{S}_J^f, \qquad f = 3, 4. \tag{43b}$$

For any boundary data, the linear system (41), with operators given by (42) and (43), can be solved for the unknown particle displacements within the domain.

5.1.1 Fault Treatment and Time-stepping

Time-stepping during the interseismic phase follows that of Erickson and Dunham (2014), where rate-and-state friction (4) is enforced on the boundary as a Dirichlet condition using fault slip. We summarize time-stepping here for completeness. We assume only the slip $\boldsymbol{\delta}$, the state variable $\boldsymbol{\psi}$ and the remote displacement $\mathbf{u}_{begin}^2$ (accrued during a previous coseismic phase) are known at time t^n. The remote boundary is slowly loaded at half the plate rate V_p and at $t = 0$ we assume $\mathbf{u}_{begin}^2$ is such that remote shear stress is τ^∞. To obtain all fields at time t^{n+1} we do the following:

1. Set the boundary data at all faces: $\boldsymbol{g}_q^{1,n} = \boldsymbol{\delta}^n/2, \boldsymbol{g}_q^{2,n} = \boldsymbol{u}_{begin}^2 + V_p(t^n - t^{begin})/2$, $\boldsymbol{g}_q^{3,n} = \boldsymbol{g}_q^{4,n} = \boldsymbol{0}$, where $\boldsymbol{u}_{begin}^2$ are particle displacements from the end of the previous coseismic period on the remote boundary and t^{begin} is the beginning time of the current interseismic period.
2. Use the boundary data to set the numerical fluxes (38), (40) and solve the linear system (41) to obtain particle displacements $\mathbf{u}^n$.
3. Use particle displacements to compute the numerical traction $\hat{\boldsymbol{\tau}}^{1,n}$ along face 1 using (39).
4. Using $\boldsymbol{\psi}^n$, equate numerical shear stress $\hat{\boldsymbol{\tau}}^{1,n}$ with fault strength via (37) and solve the nonlinear equation for slip rate $\boldsymbol{V}^n$ (done through a bracketed Newton method).
5. Use $\boldsymbol{V}^n$ and $\boldsymbol{\psi}^n$ to explicitly integrate $\boldsymbol{\delta}$ and $\boldsymbol{\psi}$ one time-step, according to (2) and (5). We apply the adaptive, 4th order Runge-Kutta scheme `Tsit5()` in the Julia programming language (Bezanson et al., 2017; Julia Scientific Machine Learning, 2022) and obtain updated slip $\boldsymbol{\delta}^{n+1}$ and state $\boldsymbol{\psi}^{n+1}$, then return to step 1.

Note that the adaptive nature of the time-stepping method enables large time-steps during interseismic loading when $\boldsymbol{V}$ is close to zero, that decrease in size as rupture nucleates.

5.2 The Coseismic Phase

During the coseismic phase, in which particle accelerations are substantial, arbitrary explicit time-stepping methods may be applied to the elastodynamic wave equation (11). To spatially discretize we apply (34), enforcing boundary conditions (16) again through numerical fluxes using the techniques of Erickson, Kozdon, and Harvey (2022, Section 5.1), which include a characteristic, non-stiff implementation of rate-and-state friction at the fault.

5.2.1 Boundary Conditions

During dynamic rupture, we set the remote and depth boundary conditions to be non-reflecting so that waves can freely exit the finite computational domain. The reflection coefficients in (9) on these two faces (faces 2 and 4) are taken to be $R^2 = R^4 =$

0 and the boundary data g_d^2, g_d^4 will be specified shortly when we link the interseismic and coseismic phases together. As in the interseismic phase, Earth's free surface lies at $z = 0$, and rate-and-state friction on the fault is imposed through a characteristic condition on face 1. These latter assumptions correspond to zero boundary data at the fault and a free surface in equation (9), namely $g_d^1 = g_d^3 = 0$, however the reflection coefficient at the fault (face 1) is not constant, but is rather implicitly defined through choices of numerical fluxes and therefore imposes friction.

The main idea behind the characteristic boundary condition implementation is to introduce numerical fluxes $\dot{\boldsymbol{u}}^{*f}$ and $\hat{\boldsymbol{\tau}}^{*f}$ on each characteristic face f that preserve the outgoing characteristic, and also satisfy a desired boundary condition. Specifically, the fluxes must satisfy

$$\hat{\boldsymbol{Z}}^f \dot{\boldsymbol{u}}^{*f} - \hat{\boldsymbol{\tau}}^{*f} = \hat{\boldsymbol{Z}}^f \dot{\boldsymbol{u}}^f - \hat{\boldsymbol{\tau}}^f, \tag{44a}$$

$$\hat{\boldsymbol{Z}}^f \dot{\boldsymbol{u}}^{*f} + \hat{\boldsymbol{\tau}}^{*f} = R^f(\hat{\boldsymbol{Z}}^f \dot{\boldsymbol{u}}^{*f} - \hat{\boldsymbol{\tau}}^{*f}) + \boldsymbol{S}_J^f \boldsymbol{g}_d^f, \tag{44b}$$

where $\hat{\boldsymbol{Z}}^f$ is the projection of the shear impedance $\hat{Z}^f$ along face f, R^f is the reflection coefficient for face f, and $\boldsymbol{g}_d^f$ is the grid projections of any characteristic boundary data.

In some cases (44) can be solved directly for the numerical fluxes: For the non-reflecting conditions, where $R^f = 0$ on faces 2 and 4, solving (44) for the fluxes results in

$$\dot{\boldsymbol{u}}^{*f} = \frac{1}{2}\left(\left(\hat{\boldsymbol{Z}}^f\right)^{-1} \boldsymbol{L}^f \dot{\boldsymbol{u}} - \hat{\boldsymbol{\tau}}^f\right) + \frac{1}{2}\boldsymbol{S}_J^f \left(\hat{\boldsymbol{Z}}^f\right)^{-1} \boldsymbol{g}_d^f, \qquad f = 2, 4 \tag{45a}$$

$$\hat{\boldsymbol{\tau}}^{*f} = -\frac{1}{2}\left(\hat{\boldsymbol{Z}}^f \boldsymbol{L}^f \dot{\boldsymbol{u}} - \hat{\boldsymbol{\tau}}^f\right) + \frac{1}{2}\boldsymbol{S}_J^f \boldsymbol{g}_d^f, \qquad f = 2, 4. \tag{45b}$$

To impose the non-characteristic Neumann boundary condition (9c), the fluxes are given simply by (40).

During the coseismic phase, rate-and-state friction is imposed through a characteristic boundary condition, coupling the fault to the volume, where the slip rate $\boldsymbol{V}$ is twice the particle velocity flux, namely $2\dot{\boldsymbol{u}}^{*1}$. The fluxes are required to satisfy (44); Equation (44a) can be replaced with the requirement that the friction law (4) be satisfied pointwise along face 1, namely

$$\hat{\boldsymbol{\tau}}^{*1} = -\boldsymbol{S}_J^1 F(2\dot{\boldsymbol{u}}^{*1}, \boldsymbol{\psi}), \tag{46a}$$

$$\hat{\boldsymbol{Z}}^1 \dot{\boldsymbol{u}}^{*1} - \hat{\boldsymbol{\tau}}^{*1} = \hat{\boldsymbol{Z}}^1 \boldsymbol{L}^1 \dot{\boldsymbol{u}} - \hat{\boldsymbol{\tau}}^1. \tag{46b}$$

Equations (46) form a nonlinear system of equations in $\boldsymbol{\tau}^{*1}$ and $\dot{\boldsymbol{u}}^{*1}$ and implicitly define a non-constant reflection coefficient $R^1 \in [-1, 1]$; see Erickson, Kozdon, and Harvey (2022). Removing any dependency on $\boldsymbol{\tau}^{*1}$, by solving (46b) and substituting the result into (46a) yields the $N + 1$ non-linear equations:

$$\hat{\boldsymbol{Z}}^1(\dot{\boldsymbol{u}}^{*1} - \boldsymbol{L}^1 \dot{\boldsymbol{u}}) + \hat{\boldsymbol{\tau}}^1 + \boldsymbol{S}_J^1 F(2\dot{\boldsymbol{u}}^{*1}, \boldsymbol{\psi}) = 0, \tag{47}$$

which are solved for $\dot{\boldsymbol{u}}^{*1}$ with the same Newton method as in the solver for the interseismic period. Lastly, state $\boldsymbol{\psi}$ obeys the state evolution law (5) pointwise along the fault.

Note that with the addition of $\dot{\boldsymbol{u}}^{*f}$, N+1 ordinary differential equations (ODEs) must be integrated per face to obtain $\boldsymbol{u}^{*f}$ in (34). In total, the system (34), subject to flux conditions (45), (40), and (47), along with the state evolution law (5) form a system of second order non-stiff ODEs. In order to integrate this system we convert it to a single system of first order ODEs

$$\frac{d}{dt}\begin{bmatrix} \boldsymbol{u} \\ \dot{\boldsymbol{u}} \\ \boldsymbol{u}^{*f} \end{bmatrix} = \boldsymbol{B}\begin{bmatrix} \boldsymbol{u} \\ \dot{\boldsymbol{u}} \\ \boldsymbol{u}^{*f} \end{bmatrix}, \tag{48}$$

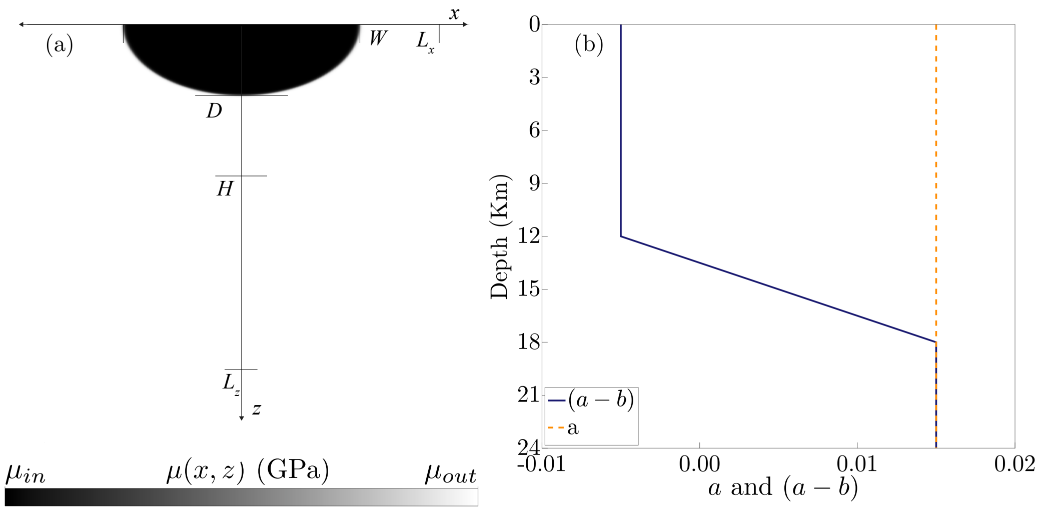

Figure 2. (a) Shear modulus within the 2D domain of our problem. The more compliant semi-ellipse is used to model a shallow sedimentary basin, that extents to a depth of D, with a width of W. The rate-and-state fault at $x = 0$ is seismogenic down to locking depth H. (b) Parameters a and $(a - b)$ vary with depth so that the fault is velocity weakening from the free surface down to a depth of ∼15 km then transitions to velocity strengthening further down dip.

and integrate it along with the state evolution equation (5) with a GPU accelerated 4th order low-storage Runga-Kutta scheme from Carpenter and Kennedy (1994, (5,4) $2N$-Storage RK scheme, solution 3) implemented in the Julia programming language (Besard et al., 2019).

6 Numerical Convergence Tests

We use the method of manufactured solutions (MMS) to empirically verify convergence (Roache, 1998) for both the coseismic and interseismic solvers. The MMS works by constructing an exact solution to the continuous problem with specific boundary and volume source terms: by plugging the exact solution into the governing equations, the source and boundary data are solved for explicitly. Convergence is then verified by comparing the numerical approximation to the exact solution.

In order to test every aspect of both numerical methods, we include a sedimentary basin as well as a coordinate transformation (detailed in Appendix A) during the convergence tests. We use the semi-ellipse from Erickson and Dunham (2014), to define the varying shear modulus,

$$\mu(x,z) = \frac{\mu_{out} - \mu_{in}}{2}\left[\tanh\left(\frac{r-\bar{r}}{r_w}\right) + 1\right] + \mu_{in}, \qquad (x,z) \in [0, L_x] \times [0, L_z], \tag{49}$$

to model the sedimentary basin; see Figure 2(a). The basin edge is defined by parameters $r = x^2 + c^2z^2$, and $c = W/2D$ for basin width W and depth D, defining a shallow compliant region characterized by shear modulus μ_{in} and transition (over a length scale r_w near $r = \bar{r}$) to a stiffer surrounding material, with shear modulus μ_{out}.

For both the coseismic and interseismic solvers we use the manufactured solution from Erickson and Dunham (2014), intended to be similar to the physical response of the problem, where the fault creeps at depth at rate V_p for several decades, until a rupture occurs within the upper, seismogenic zone. The exact displacement is taken to be

$$u_e(x,z,t) = \frac{\delta_e}{2}K(t)\phi(x,z) + \frac{V_p}{2}t\left[1-\phi(x,z)\right] + \frac{\tau^\infty}{\mu(L,y)}x, \tag{50}$$

where parameter δ_e is the amount of slip on the surface during the rupture, and τ^∞ is a prescribed stress at the remote boundary. The spatial dependency of the manufactured solution is

$$\phi(x,z) = \frac{H(H+x)}{(H+x)^2+z^2}, \tag{51}$$

where parameter H is the locking depth. The temporal dependence of the solution is given by

$$K(t) = \frac{1}{\pi}\left[\tan^{-1}\left(\frac{t-\bar{t}}{t_w}\right) + \frac{\pi}{2}\right] + \frac{V_{min}}{\delta_e}t, \tag{52}$$

where at time $\bar{t}$, the fault slip-rate increases many orders of magnitude over a short timescale t_w, simulating a rupture, and V_{min} is a parameter that sets the minimum slip rate.

Volume source term $\boldsymbol{S}$ in (34) and boundary data are derived from assume solution (50). The manufactured solution (50) determines the exact slip rate $V_e = 2\dot{u}_e$ and shear stress $\tau_e = \mu\frac{\partial u_e}{\partial x}\Big|_{x=0}$, which in turn, determine the exact state variable via the friction law (4), namely

$$\psi_e = a\ln\left(\frac{2V_0}{V_e}\sinh\left(\frac{\tau_e}{a\sigma_n}\right)\right). \tag{53}$$

Since the exact state may not satisfy (5), source data must also be added to aging law for state evolution,

$$\dot{\psi} = G(V,\psi) + \boldsymbol{S}_\psi \tag{54}$$

where

$$\boldsymbol{S}_\psi = \dot{\boldsymbol{\psi}}_e - G(V_e, \boldsymbol{\psi}_e), \tag{55}$$

and $\dot{\boldsymbol{\psi}}_e$ is determined by taking the time derivative of (53).

We let $\boldsymbol{u}_e$ be the projection of u_e onto the physical grid points and compute the error at a final time T, using the discrete H-norm, defined by

$$||\Delta\boldsymbol{u}||_{\boldsymbol{H}} = \sqrt{(\Delta\boldsymbol{u})^T\boldsymbol{J}(\boldsymbol{H}\otimes\boldsymbol{H})\Delta\boldsymbol{u}}, \tag{56}$$

where $\Delta\boldsymbol{u} = \boldsymbol{u} - \boldsymbol{u}_e$.

We verify spatial convergence of the coseismic and interseismic solvers individually using the MMS with the parameters in Table B1. For the interseismic solver we ran a simulation for $T = 70$ years. For the coseismic solver we ran a 1-s simulation when the manufactured solution is at peak velocity between 35 years - 0.5 seconds and 35 years + 0.5 seconds. Errors and convergence rates for interior spatial order of accuracy $p = 2, 4$ and 6, with global convergence rates of 2, 4, 5, for both phases are shown in Figure 3 and Table B3 (Erickson, Kozdon, & Harvey, 2022).

7 Fully-dynamic Earthquake Sequences

Having verified that the numerical methods for the interseismic and coseismic periods are spatially convergent, we explore the effects of including full dynamics within earthquake sequence simulations with a sedimentary basin present; a follow-up study to that of Erickson and Dunham (2014). All parameters used are those from Erickson and Dunham (2014) with the shallow basin depth of $D = 4$ km, which we include in Table B4 for completeness. Rate-and-state parameters are those defined in Figure 2(b). We investigate the robustness of solutions under mesh refinement, different switching criteria, the characteristics of the resulting sequences, and the frequency of surface breaking ruptures over multiple cycles.

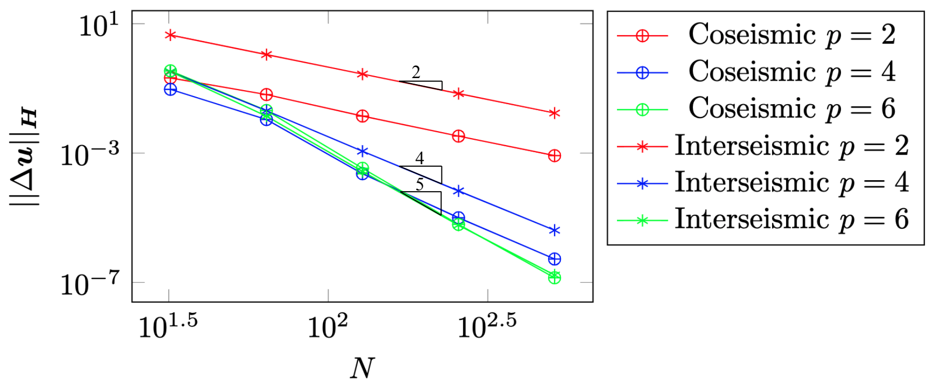

Figure 3. Convergence rates in the H-norm for the interseismic and coseismic solvers. The red, blue, and green curves correspond to SBP interior spatial order of accuracy $p = 2, 4,$ and 6, respectively, with global rates of convergence given by 2, 4, and 5.

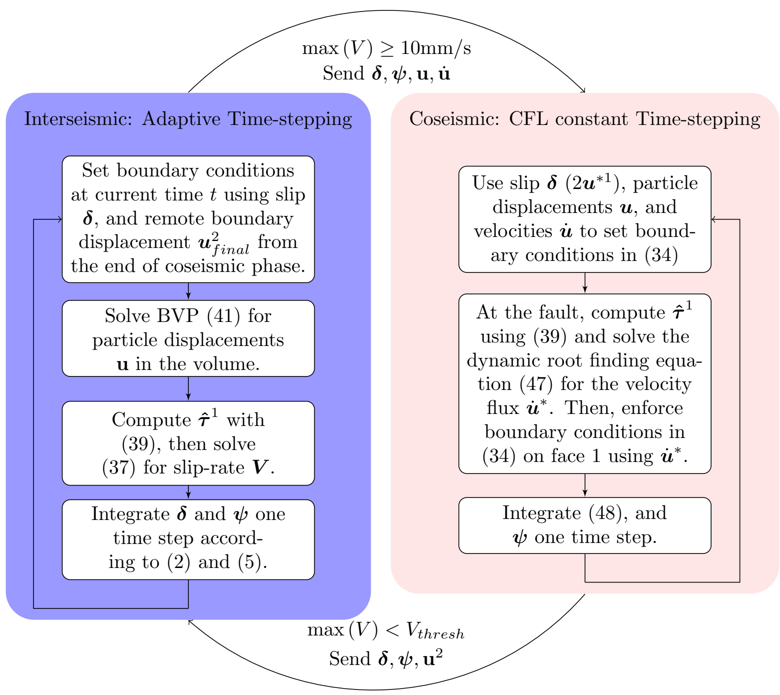

Figure 4. The overarching numerical algorithm involves a switch from the solver used for the interseismic phase to the coseismic (fully-dynamic) solver when $\max(V) \geq 10$ mm/s. We experiment with different thresholds when switching back to the solver for the interseismic phase, denoted by parameter V_{thresh}. When switching between interseismic and coseismic regimes, specific fields must be sent between solvers, as noted.

7.1 Initial Conditions, Switching Between Solvers, and Non-reflecting Boundary Conditions

During an earthquake sequence simulation our computational approach involves a switch between the solvers for the interseismic and coseismic (fully-dynamic) phases. Many criteria exist to determine when to switch, such as a condition on maximum slip rate, as done in Thakur and Huang (2021) or the ratio of radiating damping stress to fault shear stress (Duru et al., 2019). We elect to switch on max slip rate and find that solutions are not sensitive when switching from the interseismic to coseismic solvers using the threshold of $\max(V) > 10$ mm/s. However, we do find solutions sensitive when switching from the coseismic to the interseismic solver and address this sensitivity in Section 7.2.2. In both regimes we assume no body forces (i.e. $\boldsymbol{S} = 0$). The overarching technique for switching is outlined in Figure 4, which includes information on time-stepping during each regime, as well as an overview of which fields are sent in order to initialize the subsequent solver.

7.1.1 Interseismic Initial Conditions

At the beginning of each interseismic phase, initial conditions on slip, the state variable, and the remote displacement must be provided. At $t = 0$ we assume zero fault slip, $\delta = 0$, and remote displacement is set by setting the Dirichlet boundary data $g_q^2(z, 0) = \tau^\infty L_x/\mu(L_x, z)$ as done in Erickson and Dunham (2014). Initial state is set such that initial slip rate on the fault is V_p and shear stress on the fault is equal to τ^∞, namely

$$\psi(z, 0) = a \ln\left[\frac{2V_0}{V_p}\sinh\left(\frac{\tau^\infty - \eta V_p}{\sigma_n a}\right)\right]. \tag{57}$$

When switching back to the interseismic phases at later points in the simulation, slip and state are initialized by the final conditions from the previous coseismic phase, as detailed in the time-stepping scheme in Section 5.1. In addition, the coseismic phase produces waves in the bulk which displaces the remote boundary. The final remote displacement is also passed to the interseismic solver at the beginning of an interseismic phase. Namely, we set

$$\boldsymbol{\delta}_{begin} = 2\boldsymbol{u}^{*1}_{final}, \tag{58a}$$
$$\boldsymbol{\psi}_{begin} = \boldsymbol{\psi}_{final}, \tag{58b}$$
$$\boldsymbol{u}^2_{begin} = \boldsymbol{u}^2_{final}, \tag{58c}$$

where the final conditions of the last coseismic phase are denoted with a subscript $final$ and the initial conditions of the next interseismic phase with subscript *begin*. The interseismic phase is then integrated in time using the technique described in Section 5.1.1, until an event nucleates.

7.1.2 Coseismic Initial and Boundary Conditions

The coseismic solver requires initial conditions on particle displacements and velocities, as well as on the state variable and all numerical fluxes on the four faces, $\boldsymbol{u}^{*f}$. Since particle displacements, slip, and state ψ are computed at each time-step of the interseismic phase, these can be passed directly to the coseismic solver. The remaining fluxes $\boldsymbol{u}^{*f}$ are set by restricting the particle displacement to each face. A backwards difference approximation is used to compute initial particle velocities. These choices correspond to the conditions

$$\boldsymbol{u}_{begin} = \boldsymbol{u}_{final}, \tag{59a}$$
$$\dot{\boldsymbol{u}}_{begin} = \frac{\boldsymbol{u}_{final} - \boldsymbol{u}_{final-1}}{t_{final} - t_{final-1}}, \tag{59b}$$
$$\boldsymbol{u}^{*1}_{begin} = \boldsymbol{\delta}_{final}/2, \tag{59c}$$
$$\boldsymbol{u}^{*f}_{begin} = \boldsymbol{L}^f \boldsymbol{u}_{final}, \qquad f = 2,3,4, \tag{59d}$$
$$\boldsymbol{\psi}_{begin} = \boldsymbol{\psi}_{final}. \tag{59e}$$

In Section 5.2.1 we provided information on all the boundary data except for those at the non-reflecting boundaries (faces 2 and 4). In usual settings, non-reflecting boundary conditions would require that the boundary data satisfy $g^2_d(z,t) = g^4_d(x,t) = 0$. However, the initial conditions from the previous interseismic phase do not necessarily satisfy the non-reflecting conditions with zero boundary data (i.e. $\boldsymbol{Z}^f \bar{\boldsymbol{L}}^f \dot{\boldsymbol{u}}_{begin} + \hat{\boldsymbol{\tau}}^f_{begin} \neq 0$, $f = 2,4$), which can send an erroneous wave into the domain from these boundaries. This could be accounted for this by considering the coseismic phase in terms of perturbations from the final conditions of the interseismic phase or by applying the superposition principle and using the final conditions from the interseismic phase to set the non-reflecting boundary data. We choose the latter technique, namely letting

$$\boldsymbol{g}^f_d = \boldsymbol{Z}^f \bar{\boldsymbol{L}}^f \dot{\boldsymbol{u}}_{begin} + \hat{\boldsymbol{\tau}}^f_{begin}, \qquad f = 2,4, \tag{60}$$

so that throughout the coseismic period any discrepancy between the initial data and boundary conditions is accounted for and perturbations in excess freely exit the domain.

7.2 Sensitivity to Computational Parameters

With all boundary and initial conditions set, we investigate the dependence of solutions on both grid resolution and coseismic to interseismic switching criteria. Ideally, simulations with adequate grid resolution and a sufficiently stringent switching criteria should produce qualitatively similar results when all other parameters are fixed, lending confidence that we have achieved asymptotic convergence. While there is reason to believe that physics based earthquake cycle simulations can produce convergent results, there is evidence that parameter regimes exist where solutions are comparable for the first few cycles but eventually diverge, regardless of numerical resolution (Lambert & Lapusta, 2021). We first explore how solutions produced by our method are sensitive to grid resolution with three different experimental setups. We consider the same parameters as Erickson and Dunham (2014), with a 4 km deep basin with interior shear modulus $\mu_{in} = 8$ GPa with one exception: to make the grid refinement tests computationally feasible we consider $L = 32$ mm (enhanced from the 8 mm of Erickson and Dunham (2014)). Next we test three switching criteria with fixed grid resolution for both $L = 32$ mm and $L = 8$ mm.

7.2.1 Convergence Under Mesh Refinement

Two physical length scales are present within all of our simulations, the critical nucleation size h^*, and the process zone Λ. The critical nucleation size determines the maximum length in a velocity weakening zone over which ruptures can spontaneously nucleate (Andrews, 1976a, 1976b; Rubin & Ampuero, 2005; Ampuero & Rubin, 2008), and is estimated to be

$$h^* = \frac{2}{\pi} \frac{\mu b L}{(b-a)^2 \sigma_n}. \tag{61}$$

A smaller length scale, known as the process zone, describes the spatial region near the rupture front under which breakdown of fault resistance occurs (Palmer & Rice, 1973; Day et al., 2005). The quasi-static process zone at a rupture speed of 0^+, Λ_0, can be estimated (Day et al., 2005; Ampuero & Rubin, 2008; Perfettini & Ampuero, 2008) as

$$\Lambda_0 = C\frac{\mu L}{b\sigma_n}, \tag{62}$$

where C is constant of order 1.

We examine the effects of resolution on both long and short time-scales in Figure 5 using $L = 32$ mm. For these simulations, $\Lambda_0 \approx 256$ m, using the minimum value of shear modulus within the basin. Figure 5 shows slip rate profiles during the fifth dynamic rupture from three different simulations of varying resolution, resolving the quasi-static cohesive zone Λ_0 with 3, 6, and 9 nodes. Slip rate is plotted against depth, at times corresponding to when the rupture tip reaches similar distances down dip (at 13.0, 13.8 and 13.6 seconds after nucleation, respectively for Figure 5(a) and 15.1, 16.0 and 15.8 s for Figure 5(b)). As seen in Figure 5(a), more spurious oscillations exist in the less resolved simulations due to numerical dispersion as the rupture tip moves up dip. When the rupture reflects off the free surface and travels back down dip these oscillations grow, see Figure 5(b). However, they remain small for the highest resolution simulation. In Figure 5(c) we plot long term maximum slip velocity over 16 event sequences for each of the three resolutions. For all three resolutions the time series are nearly identical for $\sim$1700 years. At this point the simulation with the least resolution diverges from the other two. The two finer resolution simulations diverge at $\sim$2100 years. Due to computational constraints we only test three resolutions, but we hypothesize that with increased resolution simulations will remain similar for longer time periods, but will eventually diverge due to accumulated numerical errors.

7.2.2 Sensitivity to the Switching Criterion

Similar to the previous spatial resolution tests, we are interested in the short and long term effects of an increasingly more stringent switching criteria. We elect to switch based on the maximum slip rate on the fault, $\max(V)$. We find results not sensitive to the criteria when switching from the interseismic solver to the coseismic solver and switch when $\max(V) > 10$ mm/s. However, we do see sensitivity when switching back. In Duru et al. (2019) the authors define a switching criterion based on $\max(\mathcal{R})$, where $\mathcal{R} = \eta V/\tau_{qs}$ is the (non-dimensional) ratio of the radiation damping term to shear stress on the fault. They found model results are not highly sensitive for sufficiently small values of $\max(\mathcal{R})$ and elected for a switching criteria of $\max(\mathcal{R}) = 10^{-3}$. In Figure 6 we plot time-series of surface slip for $L = 32$ m and $L = 8$ mm, during the first 18 ruptures for each simulation, and different switching thresholds of $\max(V) < 5, 1, 0.5$ mm/s. Note that a fraction of the 18 events are subbasin ruptures and do not generate surface slip; surface-rupturing events are evidenced by the almost instantaneous jumps in slip every few hundred years, with larger jumps corresponding to larger events. Figure 6(a) reveals that a higher switching threshold eventually diverges from the two more stringent criteria. However, we compute $\max(\mathcal{R})$ at the end of the 5th cycle in the $L = 32$ mm scenario, shown in the insert of Figure 6(a). Large dots represent the time at which there is a switch from the coseismic to the interseismic solver. Regardless of the when the switch takes place, the value of $\max(\mathcal{R})$ remains similar throughout the rupture, as in Duru et al. (2019), for sufficiently small threshold values. We hypothesize that events early on in a simulation may show such insensitivity to the switching threshold, however, our results demonstrate that sensitivity to the threshold may manifest later on in the earthquake cycle. Additionally, in Figure 6(b) we show long term time-series of surface slip for the $L = 8$ mm case. The two more stringent thresholds give comparable results, whereas the criteria $\max(V) < 5$ m/s again yields divergent results. Also illustrated in the same figure is that the higher switching threshold generates surface-rupturing events of different sizes, evidenced by the smaller events that appear around 1300 years.

If two different thresholds are used to switch from the coseismic to interseismic solver, it could be that the initial conditions produced for the subsequent dynamic rupture are

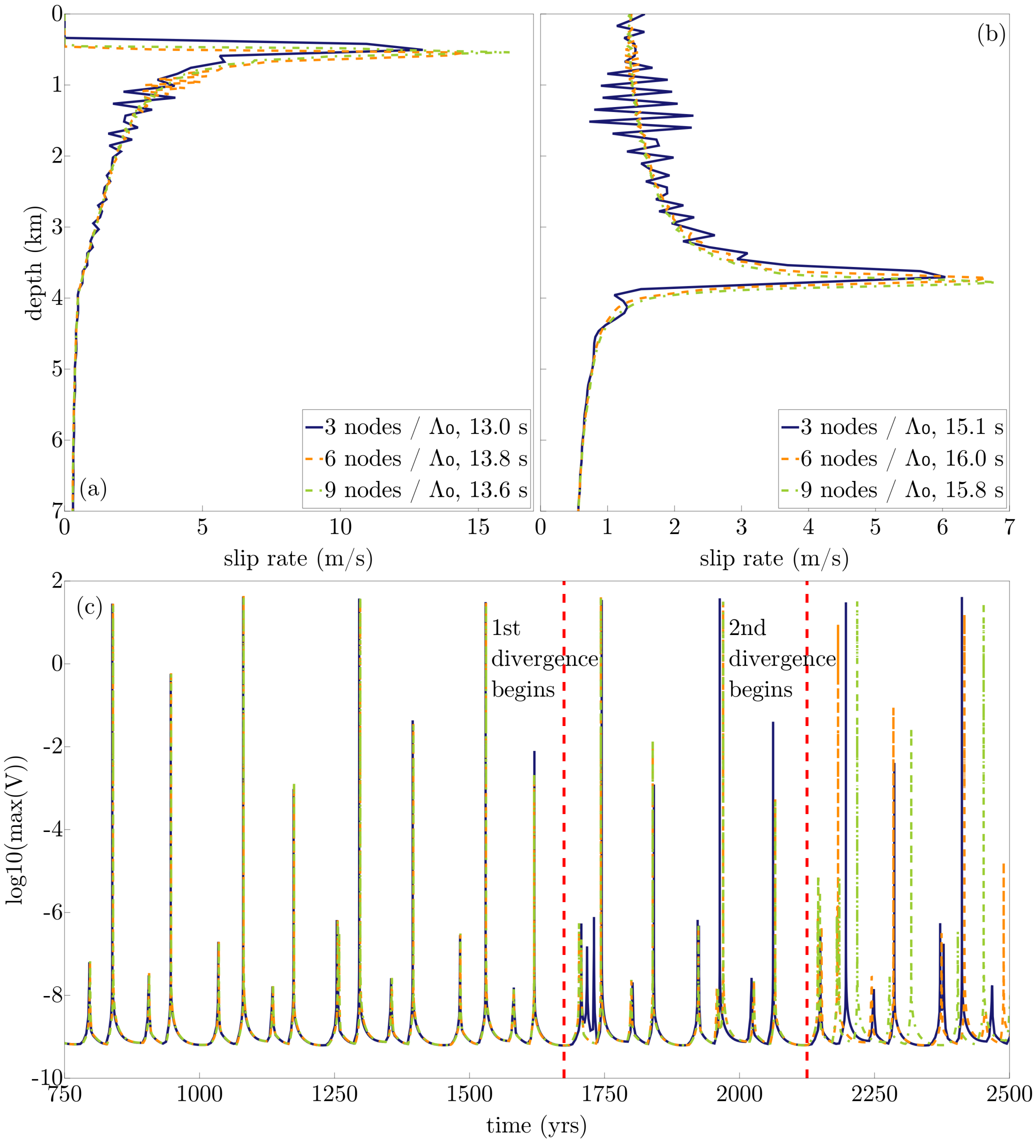

Figure 5. Slip rates along the fault during a rupture propagating (a) up-dip and (b) down-dip. Data are aligned in space for comparison but correspond to different times following the start of the coseismic phase, noted in seconds in the legends. (c) Time series of max slip rate on the fault during the first ∼ 1700 years following the spin up period. Red dotted lines indicate where the less resolved solutions begin to diverge from the others.

similar enough that the qualitative characteristics of the rupture are nearly identical. For instance the different modeling simulations included in the community code verification tests of Erickson, Jiang, et al. (2022) involved different switching criteria which we found had little impact on long term qualitative rupture characteristics for a homogeneous problem similar to the one we consider in this work. We also find that the switching criteria for the homogeneous version of our problem (i.e. without the sedimentary basin) has little impact on the long term qualitative characteristics and we do not observe long-term divergence using different thresholds. The divergence illustrated in Figure 6 illustrates that the switching criteria can drastically affect longer term rupture characteristics when material heterogeneities are present.

8 Fully-dynamic Multi-Cycle Simulation

Using $L = 8$ mm, a sufficiently stringent switching criteria of $\max(V) < 0.5$ mm/s, and a cohesive zone resolution of 6 nodes/Λ_0 we compare a fully-dynamic simulation with its quasi-dynamic counterpart from Erickson and Dunham (2014). In Figure 7 we plot cumulative slip profiles from both simulations, with blue contours every 5 years during the interseismic periods and in red every 0.5 seconds during dynamic rupture. We find that the addition of full dynamics does not change the alternating sequence of a buried rupture followed by a surfacing rupturing event, but fully-dynamic surface rupturing events are much larger than their quasi-dynamic counterparts. In the quasi-dynamic simulation, Figure 7(a), buried ruptures experience a maximum of $\sim$2 m of slip, and $\sim$5 m during a surface rupturing event. In contrast, the fully-dynamic simulation in Figure 7(b) experiences $\sim$2.5 m and 7 m of maximum slip, for each respective event. In addition, at the end of both a buried and surface rupturing event the final stress conditions are systemically lower in the near-surface seismogenic zone when the dynamic solver is used, as shown in Figure 8. In particular, after a surface rupturing event, the shear stress is sufficiently low within the basin, which disables the subsequent event from penetrating through, even with full dynamics present. After a subbasin rupture, stress concentrations are left at $\sim$ 2 km down dip, which assist subsequent ruptures to penetrate through the basin and reach the free surface.

Because we are interested in rupture potential to break through softer materials, in Figure 9 we plot the temporal evolution of shear stress for both a quasi-dynamic and fully-dynamic single-event rupture, both initialized with the same conditions, namely, those prior to a surface rupturing dynamic event. As observed in the figure, fully-dynamic events are accompanied with faster rupture speeds (evidenced by the speed of the crack-tip propagating up-dip), and higher levels of maximum stress (corresponding to greater slip rates and more slip). The quasi-dynamic event is unable to penetrate through the basin, even with the stress perturbation present at $\sim$1 km depth, leaving a secondary stress concentration behind, at $\sim$3 km depth. The fully-dynamic event, on the other hand, penetrates through the basin and reflects off the free surface. Interestingly, Figure 9(f) reveals that the overall stress levels at the end of the simulation period are much lower within the sedimentary basin for the fully-dynamic rupture. It is this near-surface reduction in stress that disables the next fully-dynamic rupture from penetrating to the surface.

Dynamic rupture within heterogeneous media produces variations in rupture speeds v_R, and can terminate or promote rupture (Bydlon & Dunham, 2015; Huang, 2018). In Figure 10 we plot v_r over the course of one of the surface rupturing events from Figure 7(b) along with those from the same simulation with $L = 32$ mm for comparison purposes. Rupture speed is computed by locating the maximum slip rate along the fault at adjacent time steps, and dividing through by the distance between those maximum slip rates. Since this method of computing rupture speed can be noisy, a moving average smoother is applied. Larger L implies a larger nucleation size h^*, so that events nucleate further up dip. With $L = 32$ mm, the rupture nucleates within the basin and accelerates to-

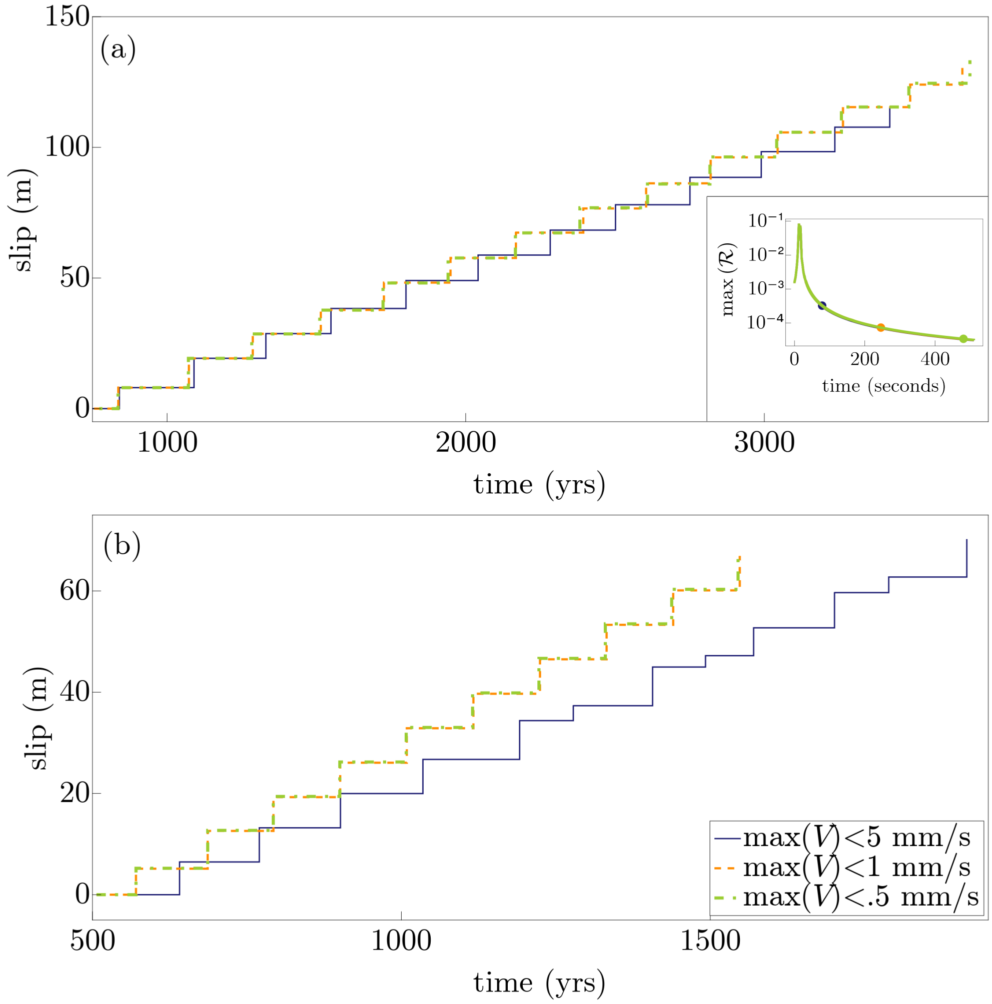

Figure 6. (a) Slip at Earth's surface during the first 18 events following the spin-up period in the $L = 32$ mm scenario with different switching criteria. The simulation with a threshold of $\max(V) < 5$ mm/s diverges quickly, and 12 surface breaking ruptures occur (the remaining 6 are subbasin events and do not produce surface slip). A total of 14 surface breaking ruptures occur in the simulations with thresholds of $\max(V) < 1$ and 0.5 mm/s, and the two simulations remain the same throughout the first ∼3500 years. (a, insert) $\max(\mathcal{R})$ during the end of the 5th rupture for the 3 different switching criteria in the $L = 32$ mm scenario. Regardless of when the switch occurs $\max(\mathcal{R})$ remains the same at the transition between rupture and the beginning of the next interseismic phase. (b) Analogous surface slip in the $L = 8$ mm scenario. The simulations with a threshold of $\max(V) < 1$ and 0.5 mm/s have 10 surface rupturing events (with the remaining 8 subbasin events), whereas the simulation with a threshold of $\max(V) < 5$ mm/s has 12 surface breaking ruptures. Again, the simulation with a threshold of $\max(V) < 5$ mm/s diverges quickly, while the other two simulations remain the same.

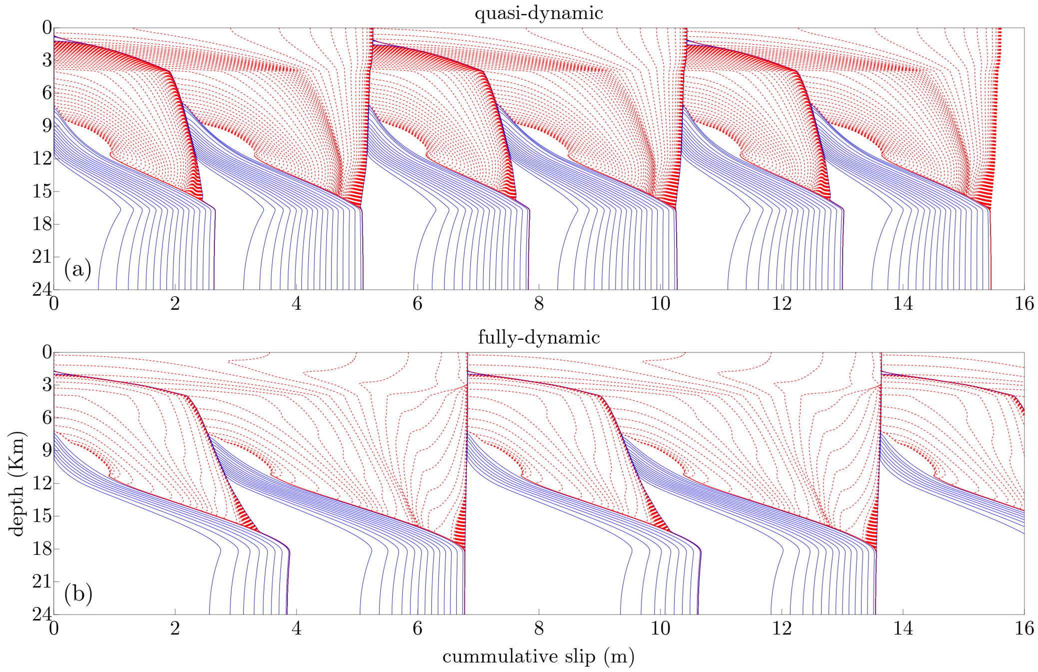

Figure 7. Cumulative slip profiles from the (a) quasi-dynamic and (b) fully-dynamic simulation with $L = 8$ mm. Each blue contour is plotted at an interval of 5 years, when the slip rate is below the switching threshold; each red contour is plotted at an interval of 0.5 seconds during the coseismic phase. Both simulations display a series of alternating buried and surface-rupturing events.

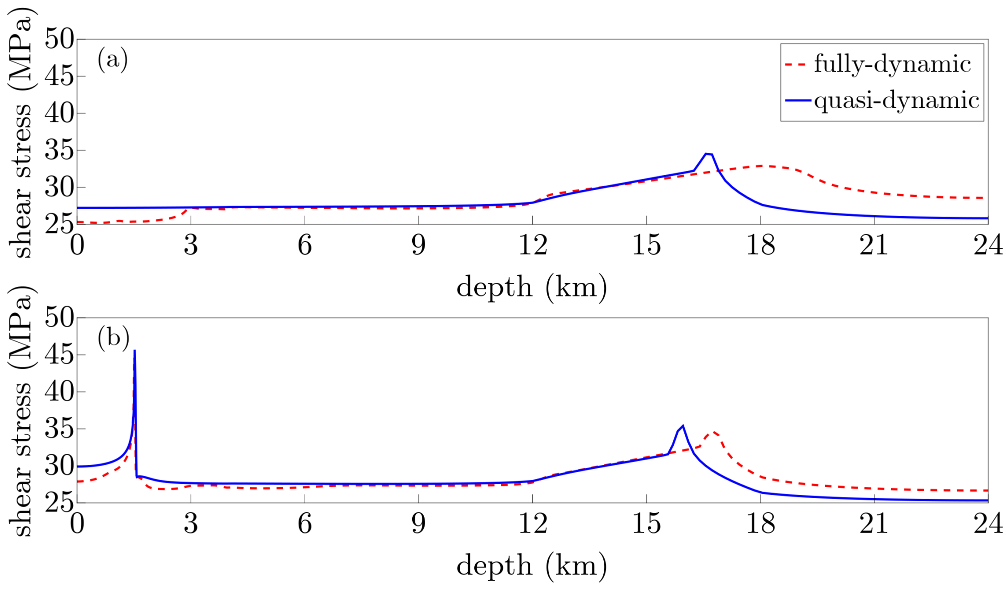

Figure 8. (a) Fault shear stress after a surface-rupturing event when integrated using the quasi-dynamic solver (solid-blue), and the fully-dynamic solver (dashed-red). (b) Fault shear stress after a buried (subbasin) rupture integrated by both the quasi-dynamic and fully-dynamic (coseismic) solver.

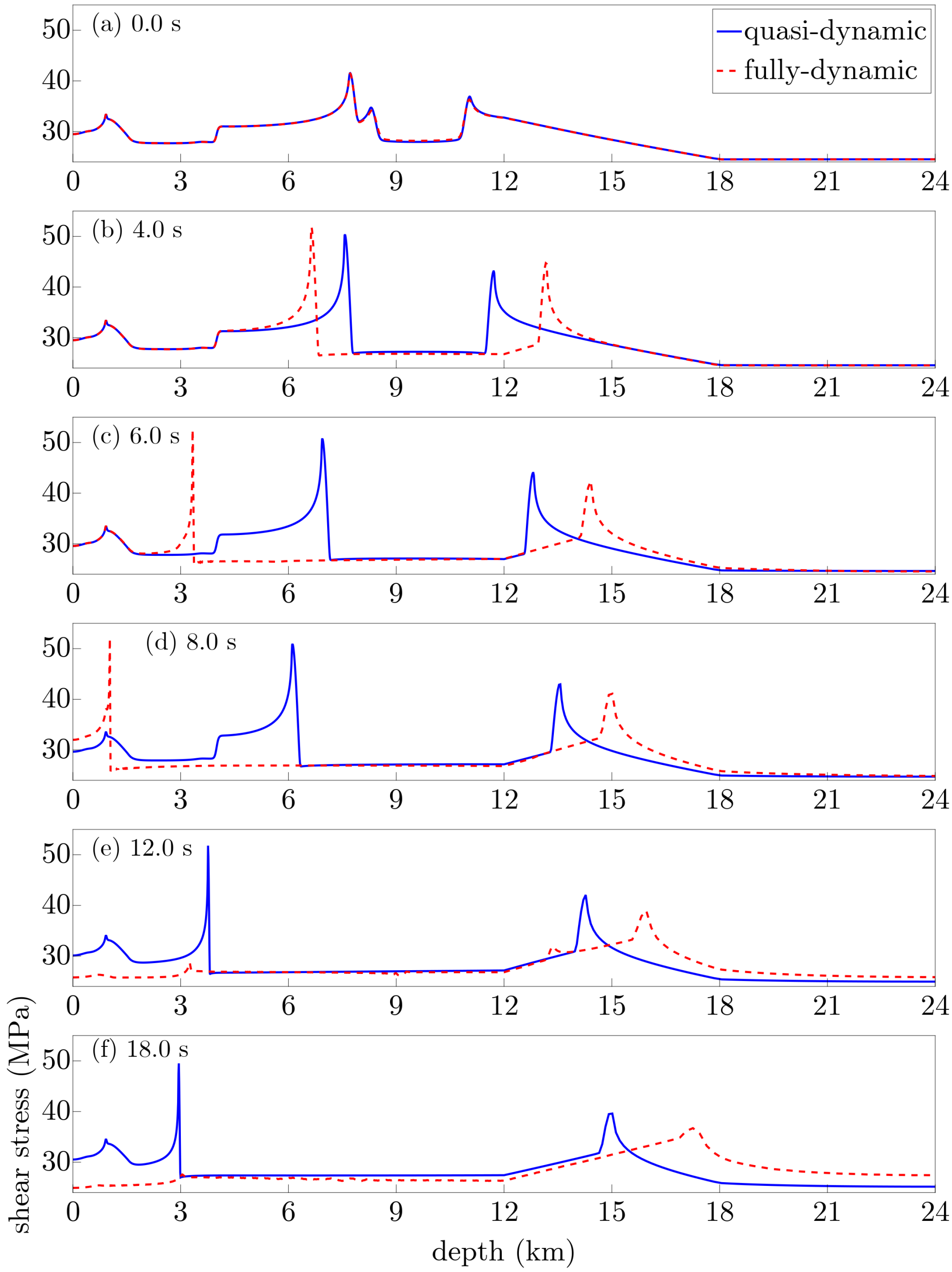

Figure 9. Fault shear stress during a quasi-dynamic (solid-blue) and fully-dynamic rupture (dashed-red). The initial conditions for both simulations are from a fully-dynamic simulation where 16 previous events were integrated using a switching criteria of $\max(V) < 0.5$ mm. The fully-dynamic solver produces a surface-rupturing event, while the rupture produced by the quasi-dynamic solver does not penetrate through the basin but rather terminates at ~ 3 km depth.

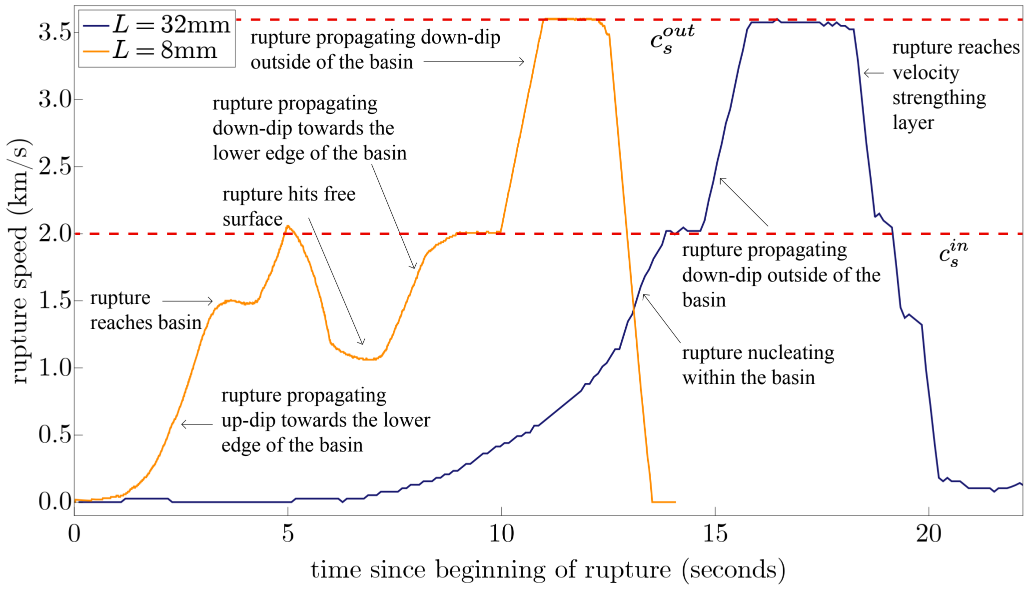

Figure 10. Rupture speeds during a surface rupturing event for $L = 32$ mm (blue), and $L = 8$ mm (yellow). The rupture with $L = 32$ mm nucleates inside the basin and briefly propagates at c_s^{in}, then exits the basin and propagates at c_s^{out}. With $L = 8$ mm, the rupture nucleates below the basin and accelerates, entering the basin soon after. It reflects off the free surface and propagates down dip through the basin at c_s^{in} and then further down-dip at c_s^{out}.

wards the surface, bounded by the basin shear wave speed $cs_s^{in} = 2$ km/s. Eventually the rupture reaches the surface and on the decent from the surface v_R reaches c_s^{in} at about 15 seconds. As it exits the basin, the rupture accelerates further, attaining the exterior shear wave speed $c_s^{out} \approx 3.6$ km/s. In the $L = 8$ mm scenario, the rupture nucleates below the basin, accelerating towards c_s^{out} initially, then slows down within the basin. After hitting the surface, the rupture eventually reaches c_s^{in} as it propagates back downwards, and as it leaves the basin it increases to c_s^{out}. In both scenarios rupture speeds accelerate and decelerate in response to the heterogeneous material properties, creating scattering in the bulk.

Finally, we illustrate features of rupture properties in such heterogeneous media through a well-resolved simulation. For the $L = 8$ mm scenario we showcase rupture propagation and scattering of waves in the bulk for one of the surface rupturing events from Figure 7(b) in Figure 11, plotted at representative times during rupture, relative to the start of the event. At $t = 5.5$ s, the event has nucleated and is below the 4-km deep basin and propagating up-dip. The event reaches the basin edge 0.5 s later, with shear waves propagating into the basin at a reduced speed to the wave front propagating outside the basin. By 8.5 s the rupture has reached the free surface; reflections off the free surface and remote basin edges propagate throughout the basin. At 10 s the rupture propagates down dip and sends out more shear waves into the basin, which are both reflected and transmitted at basin edges. By 11 and 13 s Figure 11(e) and 11(f), rupture has exited the basin, sending out waves at increased shear wave speeds than those propagating inside the basin.

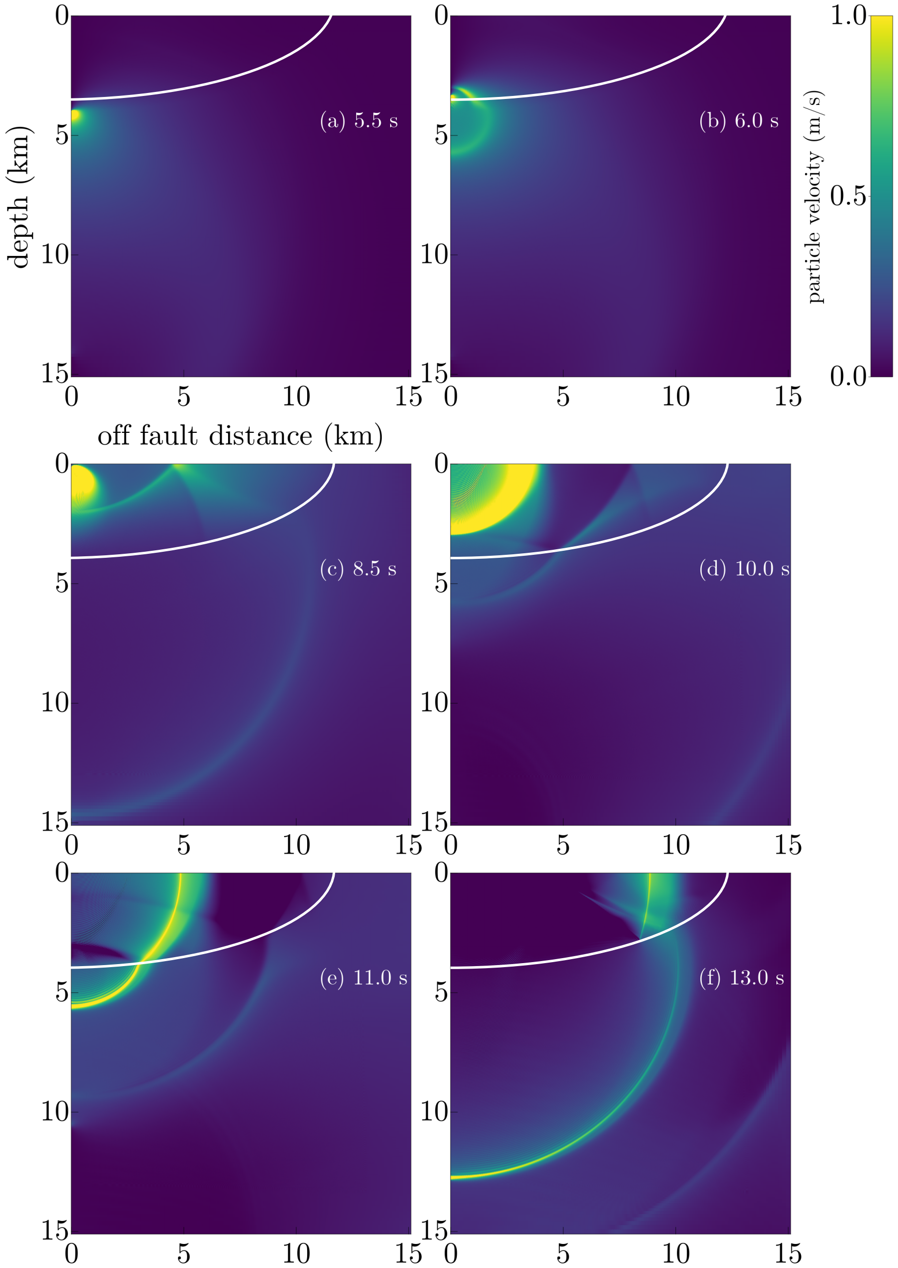

Figure 11. Particle velocities within the bulk with time relative to nucleation: (a) the event nucleates below the basin, at about 4.5 km down dip and propagates upwards towards the basin edge (semi-ellipse in white contour). (b) Shear waves emitted from the fault propagate within and outside the basin at their respected shear-wave speeds. (c) Shear waves reflect off the free surface as rupture approaches. (d) Rupture propagates down-dip and through basin as shear waves reflect off and transmit through basin edges. (e) The rupture propagates down-dip and through the basin. (f) The rupture tip moves towards the velocity strengthening region nearing the end of the event.

9 Summary and Discussion

We have developed a non-stiff, fully-dynamic numerical method for simulating sequences of earthquake cycles on a strike-slip fault in heterogeneous media with rate-and-state friction. Our method is developed with a high-order accurate, SBP-SAT spatial discretization based on Erickson, Kozdon, and Harvey (2022) for the coseismic period, and adapted to address the interseismic periods. The computational framework incorporates the time-stepping algorithm from the quasi-dynamic approach in Erickson and Dunham (2014), while the non-stiff dynamic method enables the use of general explicit time stepping methods. The addition of a dynamic solver takes into account wave mediated stress transfers that were not explicitly modeled in Erickson and Dunham (2014). We verify that both solution methods convergence at their theoretical rates of accuracy by using the method of manufactured solutions. In addition, our code is verified by the community code benchmark problems of Erickson, Jiang, et al. (2022), ensuring that our solutions are robust.

In this work we explored the effects of resolution of the quasi-static process zone Λ_0 on the long-term features of the earthquake cycle. We find that minimal resolution of Λ_0 match the better resolved simulations on short time scales, but eventually diverge, which is not unexpected to due accumulated numerical error. Of course, Λ_0 is an upper-bound on the smaller length scale Λ, the dynamic process zone, which shrinks to zero with increasing rupture speed v_R (Rice, 1980; Day et al., 2005). In our simulations there exist significant portions of time where the rupture is propagating at or near the (limiting) shear wave speed, as observed in Duru et al. (2019), resulting in a near-zero cohesive zone (see Figure 10). Computationally this near-zero length scale is impractical to resolve, however our tests reveal that simulations with better resolution of Λ_0 match over longer simulated time periods, suggesting that convergence with mesh refinement is achieved.

We also test the impact of the threshold when switching from the coseismic to the interseismic solver on long-term convergence. Our work is the first to study in detail model sensitivity to the switching criteria within heterogeneous media. Unlike the homogeneous case, where results do not appear very sensitive, we find that different thresholds can result in model divergence on long time scales. Because we consider heterogeneous material properties, a possibly more appropriate switching criteria might be based on maximum particle velocity v within the domain as seismic waves reflect off the edges of the sedimentary basin and propagate back to the fault. However, because our remote boundary conditions during the coseismic phase are not perfectly absorbing, and the fact that we don't implement any numerical dissipation, elastic waves in the bulk never dampen below a reasonable threshold of $\max(v) < 5$ mm/s rendering it impossible to explore sensitivity to more stringent switching criteria. However, maximum slip rates on the fault still define a good proxy for amplitudes of waves in the bulk, since waves emitted from the fault would not be larger than half the slip rate.

As shown in Figure 6(b), a higher switching criteria of $\max(V) < 5$ mm/s yields divergent results in the long-term time-series, corresponding to a higher fraction of surface rupturing events. So, although all three of the cohesive zone resolution simulations eventually diverge from each other, we find that the two more stringent switching criteria remain the same for the first 18 events and hypothesis that they may remain convergent for longer simulation times. We caution however, that although these two thresholds prove sufficient for our simulations, other descriptions of heterogeneous medium may require more stringent conditions.

More stringent switching thresholds are significantly more computationally costly because they amount to longer time periods within the coseismic regime where small time steps subject to the CFL condition are required. In future work it may be beneficial to move away from methods requiring an abrupt switch between solvers, but rather apply a fully implicit, or implicit-explicit (IMEX) time stepping method (Ascher et al., 1995). With an IMEX method, the fully-dynamic scheme could be used in both the coseismic and interseismic periods, providing a seamless transition between regimes. In this setting fault fluxes could be integrated explicitly, avoiding any need to solve a non-linear system of equations, while the volume terms could be integrated implicitly and adaptively during interseismic periods. During ruptures the volume terms could also me integrated explicitly for better computational efficiency.

The main objective of this work was to revisit the quasi-dynamic results of Erickson and Dunham (2014). We compare simulations results with full dynamics present, assuming a sedimentary basin depth of 4 km. Because single-event dynamic simulations are known to be capable of penetrating farther into sedimentary regions, we hypothesized that fully-dynamic simulations would see an increased frequency of surface rupturing events. However, both modeling scenarios lead to an alternating sequence of subbasin and surface rupturing events, with larger rupture speeds, slip rates and total slip accompanying the fully-dynamic simulation. The subbasin events in the fully-dynamic simulations were made possible by previous, surface rupturing events that left a reduced shear stress within the shallow basin.

To probe rupture potential to penetrate into regions unfavorable for slip we initialize a quasi-dynamic simulation with initial conditions from a dynamic surface breaking rupture and find that the quasi-dynamic simulation cannot penetrate through the basin. This observation compliments those of Kozdon and Dunham (2013), and Lambert and Lapusta (2021) who showed that full dynamics can promote rupture into areas unfavorable for slip. While these works considered velocity-strengthening barriers and/or shallow sedimentary regions, our findings isolate the effects of sediments: while velocity strengthening zones can act as a barriers to rupture, so can sediments alone, even with full dynamics present. While fully-dynamic simulations generate stronger ruptures, it is not the case that surface rupturing events will occur at a higher frequency. Instead, because the large surface rupturing event reduces the residual shear stress within the basin, the subsequent event is a sub-basin rupture and the dynamic simulations retain the alternating limit cycle as seen in the quasi-dynamic simulations. These results suggest that it is not enough to run a single dynamic rupture simulation in order infer rupture potential into and through regions that might be unfavorable for slip. Initial conditions left by a long history of seismic cycling must be considered.

10 Data Availability Statement

The code used to perform all numerical simulations is written purely in the Julia programming language and is available at: `https://github.com/Thrase/Basin_Simulations`.

Appendix A Simulation Coordinate Transformation

In order resolve the length scales presented in Section 7.2.1 with minimal addition of spatial nodes the following coordinate transformation is applied:

$$x(r) = A \tanh\left(\frac{r-1}{l}\right) + B(r-1) + C, \tag{A1a}$$

$$z(s) = A \tanh\left(\frac{s-1}{l}\right) + B(s-1) + C, \tag{A1b}$$

$$\tag{A1c}$$

where

$$A = \frac{L(\hat{r}-1)}{2\tanh\left((\hat{r}-1)/l\right) + \tanh(-2/l)(\hat{r}-1)}, \tag{A2a}$$

$$B = \frac{A\tanh(-2/l)}{2}, \tag{A2b}$$

$$C = L. \tag{A2c}$$

$$\tag{A2d}$$

These choices for parameters A, B, and C ensure that the mapping is conformal and includes evenly spaced nodes down to a depth of $\hat{r}L$, where $L = L_x = L_z$ in all of our simulations. Parameter l determines the aggressiveness of grid stretching beyond $\hat{r}L$.

Appendix B Convergence Rates and Simulation Parameters

Convergence rates for both the interseismic and coseismic solvers during the MMS tests are given in Tables B2 and B3, along with parameters used in Table B1, and B4.

parameter	value
L_x, L_z	40 km
H	8 km
D	6 km
$\bar{r}$	$(W/2)^2$ km
r_w	30 km
μ_{in}	18 GPa
μ_{out}	24 GPa
ρ_{in}	2.6 kg/m^3
ρ_{out}	3.0 kg/m^3
σ_n	50 MPa
a	.015
b	.02
L	2m
V_p	10^{-9} m/s
V_0	10^{-6} m/s
$V_{\min}$	10^{-12} m/s
t_w	10 s
$\bar{t}$	35 years
τ^∞	31.78 MPa
δ_e	1.103 m
$\hat{r}$	0.2
l	0.2

Table B1. Parameters used in manufactured solution tests for both the interseismic and coseismic solvers.

N	$\text{err}_h = \|\|\Delta \boldsymbol{u}\|\|_{\boldsymbol{H}}$	rate $\left(\log_2\left(\frac{\text{err}_{h/2}}{\text{err}_h}\right)\right)$
second-order		
2^5	2.106687e-01	
2^6	6.433138e-02	1.711318
2^7	1.393801e-02	2.206498
2^8	3.343559e-03	2.059568
2^9	8.325463e-04	2.005782
fourth-order		
2^5	9.344362e-02	
2^6	1.089363e-02	3.100611
2^7	2.303436e-04	5.563554
2^8	1.000001e-05	4.525714
2^9	5.311630e-07	4.234703
sixth-order		
2^5	3.473485e-01	
2^6	2.070132e-02	4.068589
2^7	3.391668e-04	5.931584
2^8	6.227422e-06	5.767216
2^9	1.394666e-07	5.480644

Table B2. Error and convergence rates for the coseismic solver.

N	$\text{err}_h = \|\|\Delta \boldsymbol{u}\|\|_{\boldsymbol{H}}$	rate $\left(\log_2\left(\frac{\text{err}_{h/2}}{\text{err}_h}\right)\right)$
second-order		
2^5	4.470473e+00	
2^6	1.108228e+00	2.012173
2^7	2.763847e-01	2.003505
2^8	6.904388e-02	2.001092
2^9	1.725648e-02	2.000375
fourth-order		
2^5	3.254201e-01	
2^6	2.037830e-02	3.997198
2^7	1.141190e-03	4.158423
2^8	6.750634e-05	4.079372
2^9	4.126542e-06	4.032018
sixth-order		
2^5	3.284629e-01	
2^6	1.384981e-02	4.567793
2^7	2.710573e-04	5.675124
2^8	5.863039e-06	5.530805
2^9	1.701024e-07	5.107173

Table B3. Error and convergence rates for the interseismic solver.

parameter	value
L_x, L_z	24 km
H	12 km
D	4 km
$\bar{r}$	$(W/2)^2$ km
r_w	1 + (W/2)/D km
μ_{in}	8 GPa
μ_{out}	36 GPa
ρ_{in}	2.0 kg/m^3
ρ_{out}	2.8 kg/m^3
σ_n	50 MPa
a	.015
b	depth variable
L	variable
V_p	10^{-9} m/s
V_0	10^{-6} m/s
f_0	.6
τ^∞	24.82 MPa
$\hat{r}$	0.75
l	0.05

Table B4. Parameters used in resolution tests, switching criteria tests, quasi-dynamic simulations, and fully-dynamic simulations.

References

Abdelmeguid, M., Ma, X., & Elbanna, A. (2019). A novel hybrid finite element-spectral boundary integral scheme for modeling earthquake cycles: Application to rate and state faults with low-velocity zones. *Journal of Geophysical Research: Solid Earth*, *124*(12), 12854-12881. doi: 10.1029/2019JB018036

Allison, K., & Dunham, E. M. (2018). Earthquake cycle simulations with rate-and-state friction and power-law viscoelasticity. *Tectonophysics*, *733*, 232 - 256. doi: 10.1016/j.tecto.2017.10.021

Almquist, M., & Dunham, E. M. (2020). Non-stiff boundary and interface penalties for narrow-stencil finite difference approximations of the laplacian on curvilinear multiblock grids. *Journal of Computational Physics*, *408*, 109294. doi: 10.1016/j.jcp.2020.109294

Ampuero, J.-P., & Rubin, A. M. (2008). Earthquake nucleation on rate and state faults – Aging and slip laws. *Journal of Geophysical Research: Solid Earth*, *113*(B1), 1-21. doi: 10.1029/2007JB005082

Ando, R., & Kaneko, Y. (2018). Dynamic rupture simulation reproduces spontaneous multifault rupture and arrest during the 2016 Mw 7.9 Kaikoura earthquake. *Geophysical Research Letters*, *45*(23), 12,875-12,883. doi: 10.1029/2018GL080550

Andrews, D. J. (1976a). Rupture propagation with finite stress in antiplane strain. *Journal of Geophysical Research*, *81*, 3575-3582.

Andrews, D. J. (1976b). Rupture velocity of plane strain shear cracks. *Journal of Geophysical Research*, *81*, 5679–5687.

Ascher, U. M., Ruuth, S. J., & Wetton, B. T. R. (1995). Implicit-explicit methods for time-dependent partial differential equations. *SIAM Journal on Numerical Analysis*, *32*(3), 797–823.

Barbot, S. (2018). Asthenosphere flow modulated by megathrust earthquake cycles. *Geophysical Research Letters*, *45*(12), 6018-6031. doi: 10.1029/2018GL078197

Besard, T., Foket, C., & De Sutter, B. (2019). Effective extensible programming: Unleashing julia on gpus. *IEEE Transactions on Parallel and Distributed Systems*, *30*(4), 827-841. doi: 10.1109/TPDS.2018.2872064
Bezanson, J., Edelman, A., Karpinski, S., & Shah, V. B. (2017). Julia: A fresh approach to numerical computing. *SIAM review*, *59*(1), 65–98. doi: 10.1137/141000671
Bydlon, S., & Dunham, E. (2015, 02). Rupture dynamics and ground motions from earthquakes in 2d heterogeneous media. *Geophysical Research Letters*, *42*. doi: 10.1002/2014GL062982
Carpenter, M., & Kennedy, C. (1994, 07). Fourth-order 2N-storage Runge-Kutta schemes. *Nasa reports TM, 109112,*.
Cattania, C., & Segall, P. (2021). Precursory slow slip and foreshocks on rough faults. *Journal of Geophysical Research: Solid Earth*, *126*(4). doi: 10.1029/2020JB020430
Day, S. M., Dalguer, L. A., Lapusta, N., & Liu, Y. (2005). Comparison of finite difference and boundary integral solutions to three-dimensional spontaneous rupture. *Journal of Geophysical Research: Solid Earth*, *110*(B12). doi: 10.1029/2005JB003813
Dieterich, J. H. (1979). Modeling of rock friction: 1. experimental results and constitutive equations. *Journal of Geophysical Research: Solid Earth*, *84*(B5), 2161-2168. doi: 10.1029/JB084iB05p02161
Duan, B., & Oglesby, D. D. (2007). Nonuniform prestress from prior earthquakes and the effect on dynamics of branched fault systems. *Journal of Geophysical Research: Solid Earth*, *112*(B5), 1-18. doi: 10.1029/2006JB004443
Dunham, E. M., Belanger, D., Cong, L., & Kozdon, J. E. (2011). Earthquake ruptures with strongly rate-weakening friction and off-fault plasticity, Part:2: Nonplanar faults. *Bulletin of the Seismological Society of America*, *101*(5), 2308-2322. doi: 10.1785/0120100076
Duru, K., Allison, K. L., Rivet, M., & Dunham, E. M. (2019, 07). Dynamic rupture and earthquake sequence simulations using the wave equation in second-order form. *Geophysical Journal International*, *219*(2), 796-815. doi: 10.1093/gji/ggz319
Erickson, B. A., & Dunham, E. M. (2014). An efficient numerical method for earthquake cycles in heterogeneous media: Alternating subbasin and surface-rupturing events on faults crossing a sedimentary basin. *Journal of Geophysical Research: Solid Earth*, *119*(4), 3290-3316. doi: 10.1002/2013JB010614.
Erickson, B. A., Dunham, E. M., & Khosravifar, A. (2017). A finite difference method for off-fault plasticity throughout the earthquake cycle. *Journal of the Mechanics and Physics of Solids*, *109*, 50-77. doi: 10.1016/j.jmps.2017.08.002
Erickson, B. A., Jiang, J., Barall, M., Lapusta, N., Dunham, E. M., Harris, R., … Wei, M. (2020, 01). The community code verification exercise for simulating sequences of earthquakes and aseismic slip (seas). *Seismological Research Letters*, *91*(2A), 874-890. doi: 10.1785/0220190248
Erickson, B. A., Jiang, J., Lambert, V., Abdelmeguid, M. A., Almquist, M., Ampuero, J. P., … Yang, Y. (2022). Incorporating full elastodynamic effects and dipping fault1geometries in community code verification exercises for2simulations of earthquake sequences and aseismic slip. *Seismological Research Letters*. doi: 10.31223/X5NP87
Erickson, B. A., Kozdon, J. E., & Harvey, T. W. (2022). A non-stiff summation-by-parts finite difference method for the wave equation in second order form: Characteristic boundary conditions and nonlinear interfaces. *Journal of Scientific Computing (to appear)*.
Hajarolasvadi, S., & Elbanna, A. E. (2017). A new hybrid numerical scheme for modelling elastodynamics in unbounded media with near-source heterogeneities. *Geophysical Journal International*, *211*(2), 851-864. doi:

10.1093/gji/ggx337
Harris, R. A., Aagaard, B., Barall, M., Ma, S., Roten, D., Olsen, K., … Dalguer, L. (2018). A suite of exercises for verifying dynamic earthquake rupture codes. *Seismological Research Letters*, *89*, 1146-1162. doi: 10.1785/0220170222
Harris, R. A., & Day, S. M. (1993). Dynamics of fault interaction: parallel strike-slip faults. *Journal of Geophysical Research: Solid Earth*, *98*(B3), 4461-4472. doi: 10.1029/92JB02272
Hicken, J., & Zingg, D. (2013). Summation-by-parts operators and high-order quadrature. *Journal of Computational and Applied Mathematics*, *237*(1), 111-125. doi: 10.1016/j.cam.2012.07.015
Hirono, T., Tsuda, K., & Kaneki, S. (2019). Role of weak materials in earthquake rupture dynamics. *Scientific Reports*, *9*(1), 6604.
Huang, Y. (2018). Earthquake rupture in fault zones with along-strike material heterogeneity. *Journal of Geophysical Research: Solid Earth*, *123*(11), 9884-9898. doi: 10.1029/2018JB016354
Jiang, J., Erickson, B. A., Lambert, V. R., Ampuero, J.-P., Ando, R., Barbot, S. D., … van Dinther, Y. (2022). Community-driven code comparisons for three-dimensional dynamic modeling of sequences of earthquakes and aseismic slip. *Journal of Geophysical Research: Solid Earth*, *127*(3). doi: 10.1029/2021JB023519
Julia Scientific Machine Learning. (2022). *Tsitouras 5/4 runge-kutta method.* Retrieved from `https://github.com/SciML/OrdinaryDiffEq.jl`
Kagawa, T., Irikura, K., & Somerville, P. (2004, 01). Differences in ground motion and fault rupture process between the surface and buried rupture earthquakes. *Earth Planets Space*, *56*, 3-14. doi: 10.1186/BF03352486
Kaneko, Y., Ampuero, J.-P., & Lapusta, N. (2011). Spectral-element simulations of long-term fault slip: Effect of low-rigidity layers on earthquake-cycle dynamics. *Journal of Geophysical Research: Solid Earth*, *116*(B10). doi: 10.1029/2011JB008395
Kozdon, J. E., & Dunham, E. M. (2013). Rupture to the trench: Dynamic rupture simulations of the 11 March 2011 Tohoku earthquake. *Bulletin of the Seismological Society of America*, *103*(2B), 1275-1289. doi: 10.1785/0120120136
Kozdon, J. E., Dunham, E. M., & Nordström, J. (2012). Interaction of waves with frictional interfaces using summation-by-parts difference operators: Weak enforcement of nonlinear boundary conditions. *Journal of Scientific Computing*, *50*(2), 341–367. doi: 10.1007/s10915-011-9485-3
Kreiss, H.-O., & Oliger, J. (1972). Comparison of accurate methods for the integration of hyperbolic equations. *Tellus*, *24*(3), 199-215. doi: 10.1111/j.2153-3490.1972.tb01547.x
Lambert, V., & Barbot, S. (2016). Contribution of viscoelastic flow in earthquake cycles within the lithosphere-asthenosphere system. *Geophysical Research Letters*, *43*(19), 10,142-10,154. doi: 10.1002/2016GL070345
Lambert, V., & Lapusta, N. (2021). Resolving simulated sequences of earthquakes and fault interactions: Implications for physics-based seismic hazard assessment. *Journal of Geophysical Research: Solid Earth*, *126*(10). doi: 10.1029/2021JB022193
Lapusta, N., & Rice, J. R. (2003). Nucleation and early seismic propagation of small and large events in a crustal earthquake model. *Journal of Geophysical Research: Solid Earth*, *108*(B4). doi: 10.1029/2001JB000793
Lapusta, N., Rice, J. R., Ben-Zion, Y., & Zheng, G. (2000). Elastodynamic analysis for slow tectonic loading with spontaneous rupture episodes on faults with rate- and state-dependent friction. *Journal of Geophysical Research: Solid Earth*, *105*(B10), 23765-23789. doi: 10.1029/2000JB900250
Ma, S., & Andrews, D. J. (2010). Inelastic off-fault response and three-dimensional dynamics of earthquake rupture on a strike-slip fault. *Journal of Geophysical*

Research: Solid Earth, *115*(B4).
Marone, C. (1998). Laboratory-derived friction laws and their application to seismic faulting. *Annual Review of Earth and Planetary Sciences*, *26*, 643-696.
Mattsson, K., Ham, F., & Iaccarino, G. (2009). Stable boundary treatment for the wave equation on second-order form. *Journal of Scientific Computing*, *41*(3), 366–383. doi: 10.1007/s10915-009-9305-1
Mattsson, K., & Nordström, J. (2004, 09). Summation by parts operators for finite difference approximations of second derivatives. *Journal of Computational Physic*, *199*, 503-540. doi: 10.1016/j.jcp.2004.03.001
Mattsson, K., & Parisi, F. (2010). Stable and accurate second-order formulation of the shifted wave equation. *Communications in Computational Physics*, *7*(1), 103. doi: 10.4208/cicp.2009.08.135
Noda, H., & Lapusta, N. (2010). Three-dimensional earthquake sequence simulations with evolving temperature and pore pressure due to shear heating: Effect of heterogeneous hydraulic diffusivity. *Journal of Geophysical Research: Solid Earth*, *115*(B12).
Oh, H. (2012). *Advanced fluid dynamics*. IntechOpen. Retrieved from `https://books.google.com/books?id=zH-ZDwAAQBAJ`
Palmer, A. C., & Rice, J. R. (1973). The growth of slip surfaces in the progressive failure of over-consolidated clay. *Proceedings of the Royal Society A*, *332*(1591), 527–548. doi: 10.1098/rspa.1973.0040
Perfettini, H., & Ampuero, J.-P. (2008). Dynamics of a velocity strengthening fault region: Implications for slow earthquakes and postseismic slip. *Journal of Geophysical Research: Solid Earth*, *113*(B9), 1-22. doi: 10.1029/2007JB005398
Rice, J. R. (1980). The mechanics of earthquake rupture. In *Physics of the Earth's Interior, edited by A.M. Dziewonski and E. Boschi* (pp. 555–649).
Rice, J. R. (1993). Spatio-temporal complexity of slip on a fault. *Journal of Geophysical Research*, *98*(B6), 9885–9907.
Roache, P. (1998). *Verification and validation in computational science and engineering* (1st ed.). Albuquerque, NM: Hermosa Publishers.
Rubin, A. M., & Ampuero, J.-P. (2005). Earthquake nucleation on (aging) rate and state faults. *Journal of Geophysical Research: Solid Earth*, *110*(B11), 1-24. doi: 10.1029/2005JB003686
Shaw, B. E., Milner, K. R., Field, E. H., Richards-Dinger, K., Gilchrist, J. J., Dieterich, J. H., & Jordan, T. H. (2018). A physics-based earthquake simulator replicates seismic hazard statistics across california. *Science Advances*, *4*(8). doi: 10.1126/sciadv.aau0688
Shi, Z., & Day, S. M. (2013). Rupture dynamics and ground motion from 3-D rough-fault simulations. *Journal of Geophysical Research: Solid Earth*, *118*(3), 1122-1141. doi: 10.1002/jgrb.50094
Svärd, M., & Nordström, J. (2013, 11). Review of summation-by-parts schemes for initial-boundary-value problems. *Journal of Computational Physics*, *268*. doi: 10.1016/j.jcp.2014.02.031
Thakur, P., & Huang, Y. (2021). Influence of fault zone maturity on fully dynamic earthquake cycles. *Geophysical Research Letters*, *48*(17), e2021GL094679. doi: 10.1029/2021GL094679
Thakur, P., Huang, Y., & Kaneko, Y. (2020). Effects of low-velocity fault damage zones on long-term earthquake behaviors on mature strike-slip faults. *Journal of Geophysical Research: Solid Earth*, *125*(8). doi: https://doi.org/10.1029/2020JB019587
Thomas, M. Y., Lapusta, N., Noda, H., & Avouac, J.-P. (2014). Quasi-dynamic versus fully dynamic simulations of earthquakes and aseismic slip with and without enhanced coseismic weakening. *Journal of Geophysical Research: Solid Earth*, *119*(3), 1986-2004. doi: https://doi.org/10.1002/2013JB010615
Tullis, T. E., Richards-Dinger, K., Barall, M., Dieterich, J. H., Field, E. H., Heien,

E. M., ... Yikilmaz, M. B. (2012, 11). Generic Earthquake Simulator. *Seismological Research Letters*, *83*(6), 959-963. doi: 10.1785/0220120093

Acknowledgments

T.W.H and B.A.E. were supported through National Science Foundation award EAR-2053372.